Genome-wide screening of *NEAT1* regulators reveals cross-regulation between paraspeckles and mitochondria

Yang Wang[1,5], Shi-Bin Hu [1,4,5], Meng-Ran Wang[2,5], Run-Wen Yao[1], Di Wu[1], Li Yang [2,3] and Ling-Ling Chen [1,3]*

The long noncoding RNA *NEAT1* (nuclear enriched abundant transcript 1) nucleates the formation of paraspeckles, which constitute a type of nuclear body with multiple roles in gene expression. Here we identify *NEAT1* regulators using an endogenous *NEAT1* promoter-driven enhanced green fluorescent protein reporter in human cells coupled with genome-wide RNAi screens. The screens unexpectedly yield gene candidates involved in mitochondrial functions as essential regulators of *NEAT1* expression and paraspeckle formation. Depletion of mitochondrial proteins and treatment of mitochondrial stressors both lead to aberrant *NEAT1* expression via ATF2 as well as altered morphology and numbers of paraspeckles. These changes result in enhanced retention of mRNAs of nuclear-encoded mitochondrial proteins (mito-mRNAs) in paraspeckles. Correspondingly, *NEAT1* depletion has profound effects on mitochondrial dynamics and function by altering the sequestration of mito-mRNAs in paraspeckles. Overall, our data provide a rich resource for understanding *NEAT1* and paraspeckle regulation, and reveal a cross-regulation between paraspeckles and mitochondria.

L ong noncoding RNAs (lncRNAs) are emerging as important regulators in gene expression networks. Yet, the understanding of how lncRNA genes themselves are modulated has lagged behind. The lncRNA *NEAT1* (nuclear enriched abundant transcript 1) is the main structural RNA component of paraspeckles[1–4], which are a type of nuclear body form in close proximity to the site of *NEAT1* transcription[5]. The number of paraspeckles varies in different cell types. For example, each HeLa cell contains about 10 to 30 paraspeckles. The *NEAT1* locus produces two isoforms of *NEAT1*. The long-isoform *NEAT1_2* (23,000 nt in humans) is stabilized by a triple helix structure processed by RNase P at its 3′ end, whereas the short-isoform *NEAT1_1* (3,700 nt) is polyadenylated and processed from *NEAT1_2*[2–4,6–8]. Transcription of *NEAT1* and the *NEAT1_2* isoform are essential for paraspeckle formation and maintenance[6,8,9]. In the absence of *NEAT1_2*, *NEAT1_1* alone can form 'microspeckles' that are located close to nuclear speckles[10].

Paraspeckles are organized in the form of a core–shell spheroidal structure, as revealed by electron microscopy (EM)[11] and super-resolution structural illustration microscopy (SIM)[12]. The middle region of *NEAT1_2* forms the core, which is surrounded by the 5′ and 3′ ends of *NEAT1_2* and *NEAT1_1*. More than 40 proteins are now defined as paraspeckle proteins[8,13], including NONO, SFPQ and FUS, which are exclusively co-localized with the middle region of *NEAT1_2* in paraspeckles. Under normal conditions in murine corpus luteum cells, the majority of paraspeckles appear as disperse spheroids, but a small subpopulation of paraspeckles exhibit elongated, sausage-like paraspeckles[12], which could be induced by proteasome inhibition[14].

It has been shown that mice congenitally without *NEAT1* stochastically fail to become pregnant due to defects in the formation of corpus luteum[15] and have impaired mammary gland morphogenesis and lactation[16]. At the cellular level, paraspeckles play multiple roles in gene regulation by sequestering proteins (such as SFPQ, which prevents binding to promoters of specific immune-related genes[14,17]) or mRNAs with inverted repeats (IR) in their 3′ untranslated regions (UTRs). Most of these repeats are short interspersed nuclear elements (SINEs) in mouse and *Alu* elements in human, and their retention is mediated by NONO[1,6,18–22]. The sequestration of mRNAs in paraspeckles is dynamically regulated in response to cellular stresses[18,19] and during circadian rhythm regulation[22]. Mechanistically, STAU1 outcompetes NONO binding to 3′ UTR IR*Alu*[20] or NONO methylation[21] could suppress nuclear retention of mRNAs containing IR*Alu* (IR*Alu*-mRNAs), leading to altered gene expression. Furthermore, recent genome-wide analyses have indicated that *NEAT1* also associates with active chromatin sites[13]. Despite these advances in understanding the functional implications of paraspeckles, little is known about how the *NEAT1* gene itself is regulated and how paraspeckles communicate with other cell compartments.

Here, we set up an endogenous *NEAT1* promoter-driven enhanced green fluorescent protein (EGFP) reporter cell line via transcription activator-like effector nuclease (TALEN)-mediated genome editing for genome-wide small interfering (si) RNA screening of *NEAT1* regulators, which allowed us to identify an unexpected cross-regulation between paraspeckles and mitochondria.

[1]State Key Laboratory of Molecular Biology, Shanghai Key Laboratory of Molecular Andrology, CAS Center for Excellence in Molecular Cell Science, Shanghai Institute of Biochemistry and Cell Biology, University of Chinese Academy of Sciences, Chinese Academy of Sciences, Shanghai, China. [2]Key Laboratory of Computational Biology, CAS-MPG Partner Institute for Computational Biology, Shanghai Institute of Nutrition and Health, Shanghai Institutes for Biological Sciences, University of Chinese Academy of Sciences, Chinese Academy of Sciences, Shanghai, China. [3]School of Life Science and Technology, ShanghaiTech University, Shanghai, China. [4]Present address: Department of Genetics, Stanford University, Stanford, CA, USA. [5]These authors contributed equally: Yang Wang, Shi-Bin Hu, Meng-Ran Wang. *e-mail: linglingchen@sibcb.ac.cn

Results

Genome-wide screening uncovers mitochondrial proteins as *NEAT1* regulators. To globally identify the factors regulating *NEAT1* transcription, we developed an endogenous *NEAT1*-promoter-driven EGFP reporter HeLa cell line by TALEN-mediated insertion of the *EGFP* sequence downstream of the transcription start site (TSS) of *NEAT1*. As *egfp* mRNA fusion with the nuclear retained *NEAT1* lncRNA was inefficiently exported for translation[23], we placed two copies of poly(A) sequences downstream of *EGFP* to terminate *NEAT1* transcription, and thus silenced one allele of *NEAT1* expression (Fig. 1a and Supplementary Fig. 1a). Individual clones (NEAT1[G]-HeLa) with single allele insertion were validated by genomic PCR (Fig. 1b); consistently, *NEAT1* expression remained 50% of that in wild-type (WT) cells (Fig. 1c). To exclude genes that are potentially toxic to cells during screening, we introduced the EF1α promoter-driven mCherry by lentivirus to NEAT1[G]-HeLa cells. Single clones (NEAT1[G]-HeLa-R) with EGFP expressed from the endogenous *NEAT1* promoter and mCherry as a normalization control were then used for screening to identify factors regulating *NEAT1* transcription (Fig. 1a and Supplementary Fig. 1a,b).

Next, we performed genome-wide RNAi screening with human ON-TARGETplus (OTP) siRNA libraries (Supplementary Fig. 1c). Screens were performed on 384-well plates in duplicate, and the distribution of fluorescence densities of all genes in two independent screens was highly correlated (Supplementary Fig. 1d,e). We selected candidates that could affect the activity of the *NEAT1* promoter by comparing EGFP and mCherry intensities to scramble siRNA treated NEAT1[G]-HeLa-R cells and confirmed these to be expressed in HeLa cells by analysing the available RNA-sequencing (RNA–seq) data sets (Supplementary Fig. 1f). Knockdown of 108 and 63 genes that co-occurred in both screens resulted in reduced or enhanced EGFP expression, indicating down- or upregulation of *NEAT1* transcription, respectively, while having little effect on mCherry expression (Fig. 1d and Supplementary Fig. 1f).

Gene ontology (GO) revealed the enrichment of chromatin modulators and transcription factors (TFs), as well as proteins in different organelles, as potential *NEAT1* regulators (Fig. 1e and Supplementary Fig. 1g). Among the hits located in the cytosol, nuclear encoded genes with reported roles in regulating mitochondrial functions (Fig. 1f and Supplementary Fig. 1g,h) represent the largest group of cellular factors that potentially affect *NEAT1* expression.

We randomly selected eleven candidates, including two chromatin modulators, three TFs and seven mitochondrial proteins (Supplementary Fig. 1g), for validation. The effect of each candidate on the expression of total *NEAT1* (including both short and long isoforms) was confirmed by at least two short hairpin (sh) RNAs in WT HeLa cells (Fig. 1g), suggesting high confidence for this endogenous promoter-based screening. Similar results were observed in HEK293 and U2OS cells (Fig. 1h). We also attached the *NEAT1* promoter to a promoter-less dual luciferase reporter and confirmed the results (Fig. 1i).

Loss of mitochondrial proteins leads to generation of elongated paraspeckles. Both *NEAT1* lncRNA and its transcription are essential for paraspeckle formation, and the number and morphology of paraspeckles are dynamic in cells[6,12]. We were thus drawn to examine how paraspeckle integrity would be affected following the disruption of the proteins that have an effect on *NEAT1* expression.

Paraspeckle numbers and morphologies were examined under SIM with RNA fluorescence in situ hybridization (FISH) probes[12] that target both the 5′ and 3′ regions or the middle sequence of *NEAT1_2* (Fig. 2a). HeLa cells were treated with shRNAs targeting identified *NEAT1* regulators, followed by detection of *NEAT1* expression and paraspeckle morphology. The initial SIM observations included

7 of 11 validated screening targets (Fig. 2b,c). We found that the number of paraspeckles in cells was largely correlated with the level of *NEAT1* expression in response to depletion of individual examined genes (Fig. 2c): a decreased level of *NEAT1* resulted in reduced numbers of paraspeckles, and enhanced *NEAT1* level resulted in increased numbers of paraspeckles. However, we observed distinct morphological changes in paraspeckles following knockdown of some genes. Remarkably, knockdown of nuclear genes encoding mitochondrial proteins led to about 20% increased proportion of elongated paraspeckles, yet no detectable morphological changes were found on disruption of other examined chromatin modulators or TFs, except ATF2 (Fig. 2b,c).

Similar findings were observed using a different set of shRNAs (Supplementary Fig. 2a-c). Depletion of other validated mitochondrial proteins (Supplementary Fig. 1g) also led to an increased proportion of elongated paraspeckles (Supplementary Fig. 2d,e). Similarly, ATF2 and BCL2 knockdown led to an augmented proportion of elongated paraspeckles in HEK293 cells (Fig. 2d and Supplementary Fig. 2f). Collectively, these findings reveal the involvement of mitochondrial proteins in the regulation of *NEAT1* expression and paraspeckle morphogenesis.
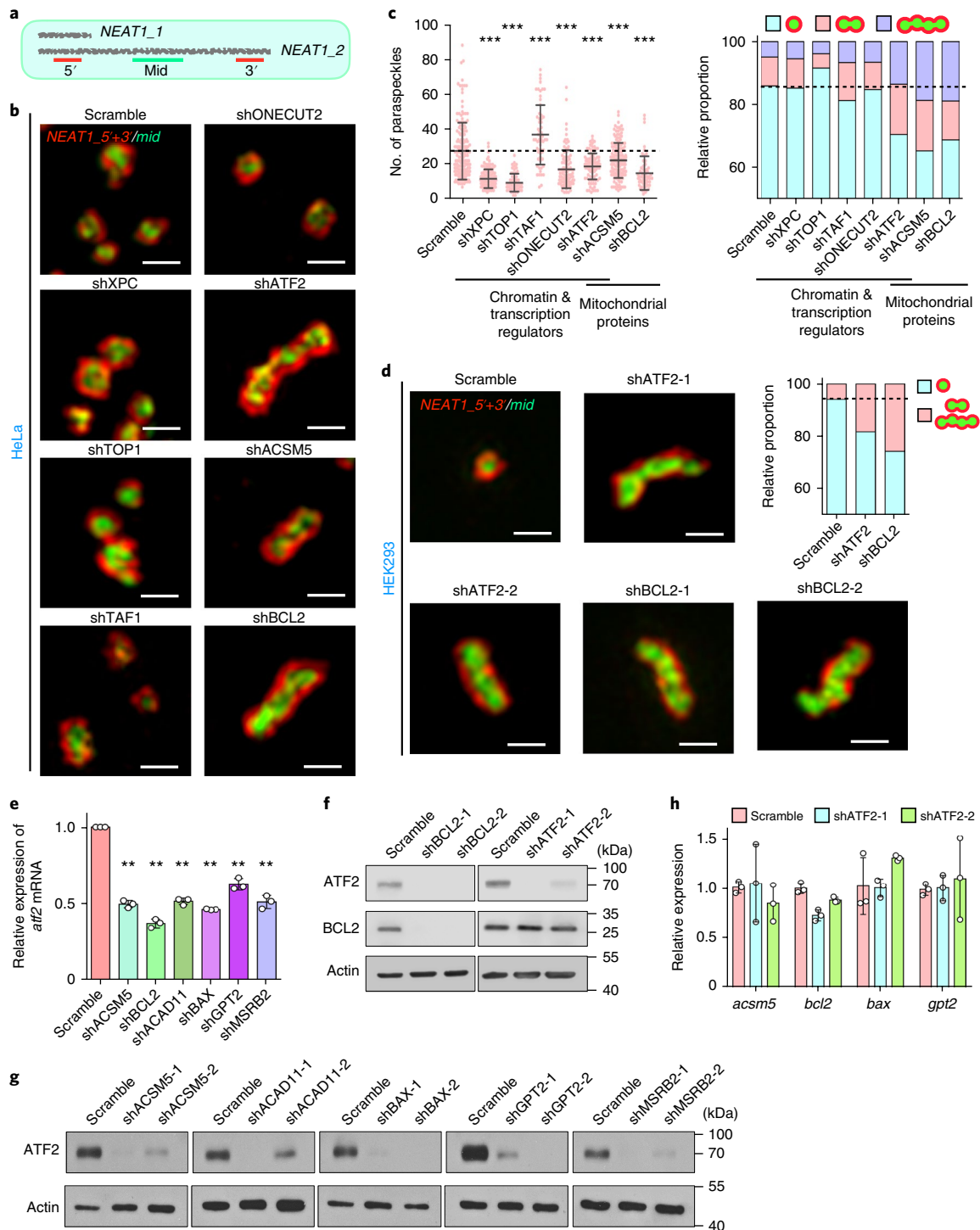
Loss of mitochondrial proteins affects *NEAT1* expression via ATF2. As mitochondrial proteins are unlikely to be direct regulators of *NEAT1* transcription in the nucleus, we speculated that TF(s) might sense the loss of mitochondrial proteins, and subsequently affected *NEAT1* expression. ATF2 is a nuclear TF activated by multiple phosphorylation sites including Thr52, Thr69 and Thr71[24,25], and mitochondrial stresses can activate ATF2[26–29]. ATF2 is also a mitochondrial protein that can increase mitochondrial permeability and promote apoptosis under genotoxic stress[25]. Such dual roles of ATF2 in the nucleus and mitochondria suggested that it might play a role in mediating mitochondria–paraspeckles (mito–paraspeckle) communication.

In keeping with this potential role, both the mRNA and protein levels of ATF2 were remarkably reduced in response to loss of mitochondrial proteins that have an impact on *NEAT1* transcription (Figs. 1 and 2e–g and Supplementary Fig. 3a,b). These proteins play important roles in mitochondrial functions (Supplementary Fig. 1h), including the mitochondrial pathway of apoptosis (BCL2 and BAX[30]), fatty acid metabolism (ACSM5[31] and ACAD11[32]), metabolism of glucose and amino acids (GPT2[33]) and oxidative stress (MSRB2[34]). As disruption of ATF2 had no detectable effect on the expression of BCL2 (Fig. 2f) and several other examined mitochondrial proteins (Fig. 2h), we speculated that ATF2 could act as a downstream sensor of mitochondrial signals to modulate *NEAT1* transcription as a TF. Note that not all observed *NEAT1* reduction following the loss of cellular proteins was ATF2-dependent. For example, loss of PPRC1, a protein involved in mitochondrial biogenesis[35], or depletion of ERLIN2, another screening hit of *NEAT1* repression localized to endoplasmic reticulum, had little effect on ATF2 (Supplementary Fig. 3c,d).

Next, we asked whether ATF2 could directly act on *NEAT1* transcription. First, analysis of the *NEAT1* promoter revealed a consensus ATF2 binding site, called the cyclic adenosine monophosphate (cAMP) response element (CRE, 5′-TGACGTCA-3′)[36,37], located 536 bp upstream of the *NEAT1* TSS (Fig. 3a). Second, ATF2 chromatin immunoprecipitation (ChIP) assays revealed that ATF2 was enriched on the *NEAT1* promoter near CRE (Fig. 3a). Third, we cloned WT or CRE-deleted *NEAT1* promoter to the upstream of a promoter-less luciferase reporter. The luciferase mRNA transcribed from the CRE site-deleted *NEAT1* promoter was reduced compared to that from the WT promoter (Supplementary Fig. 3e). Sodium arsenite (SA) is a known mitochondrial stressor that can trigger oxidative stress and activate ATF2[28,29]. So next we tested whether ATF2-regulated *NEAT1* expression was affected by SA stimulation.
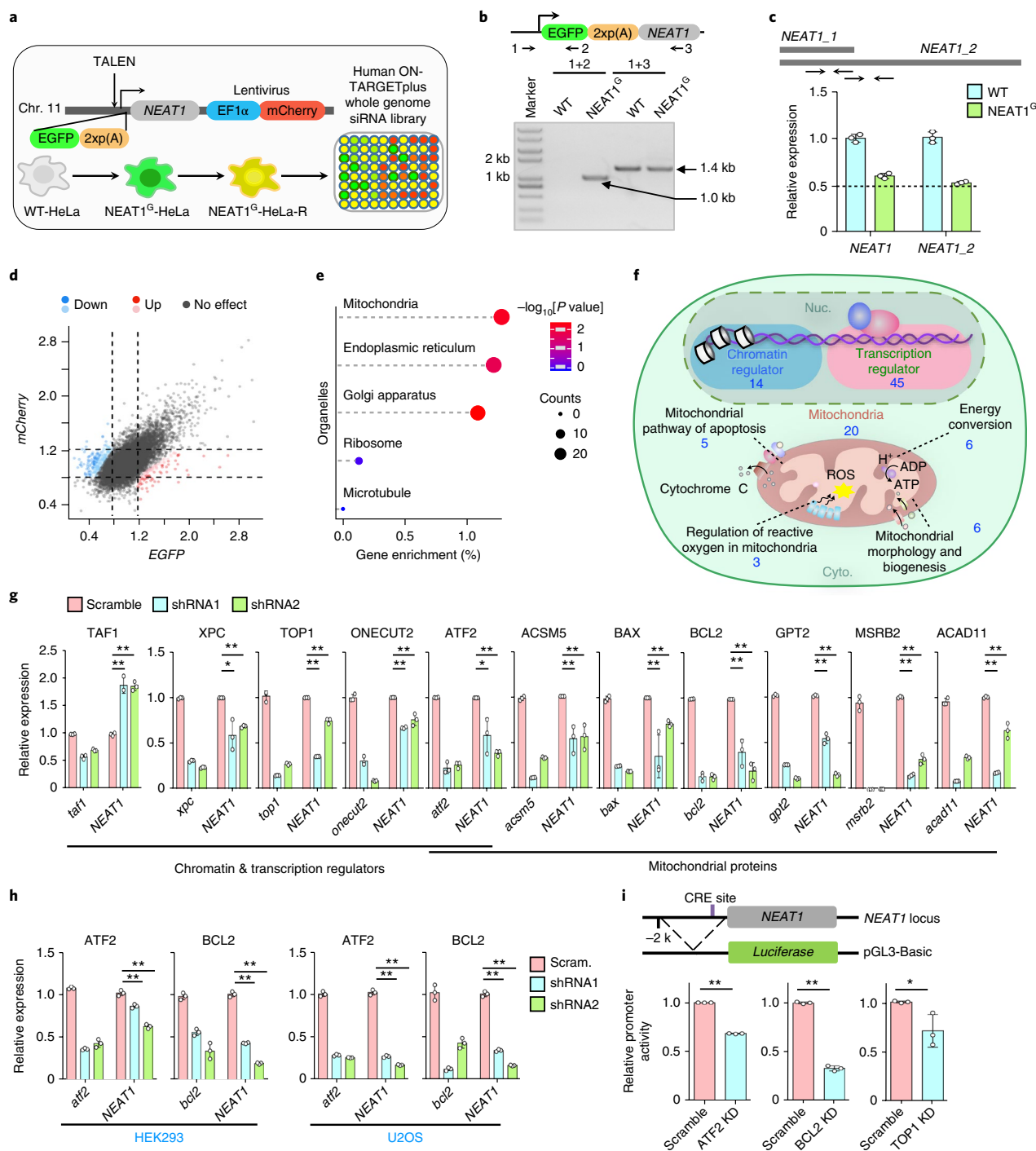
Fig. 1 | Genome-wide screening uncovers mitochondrial proteins as *NEAT1* regulators. a, Workflow to generate the TALEN-mediated NEAT1[G]-HeLa-R cell lines and the strategy of screening. **b**, Top, Schematic drawing of the EGFP-2×p(A) inserted into the endogenous *NEAT1* locus. Primers used for PCR are indicated by arrows. Bottom, PCR of the genomic DNA extracted from NEAT1[G]-HeLa clones confirmed that EGFP-2×p(A) was inserted into the promoter region of one *NEAT1* allele. Data shown represent results from four independent experiments. **c**, RT–qPCR validation of both total *NEAT1* and long isoform *NEAT1_2* expression in WT and NEAT1[G]-HeLa cells; two *NEAT1* isoforms and primer sets used are indicated on the top ($n = 3$ independent experiments). **d**, Results of human ON-TARGETplus (OTP) RNAi screenings, shown by plotting the averaged fluorescence intensities of EGFP over mCherry of individual siRNA-targeted genes obtained from two independent experiments. **e**, Enrichment of gene candidates from RNAi screenings in cellular organelles. The *x* axis shows the ratio of the number of genes in a given organelle divided by the total number of gene candidates from **d** (one-sided Fisher's exact test). The *y* axis shows the category of organelles. **f**, Summary of screening candidates involved in regulation of *NEAT1* transcription. Candidates with reported roles in chromatin modulation, transcription regulation and mitochondrial function are listed. **g**, Validation of screening candidates by shRNAs in WT HeLa cells ($n = 3$ independent experiments). ROS, reactive oxygen species. **h**, Validation of screening candidates ATF2 (activating transcription factor 2) and BCL2 (B-cell lymphoma 2) by shRNAs in HEK293 and U2OS cells ($n = 3$ independent experiments). **i**, Dual luciferase reporter assays confirmed that randomly selected targets could regulate the activity of *NEAT1* promoter. The vector used is shown on the top ($n = 3$ independent experiments). KD, knockdown. Data in all bar graph are presented as mean ± s.d. *P* values in **g–i** are calculated using two-tailed unpaired Student's *t*-test; *$P < 0.05$; **$P < 0.01$. Statistical source data, including precise *P* values for **c**, **e**, **g–i**, are provided in Supplementary Table 6. Unprocessed blots for **b** are shown in Supplementary Fig. 8.

Fig. 2 | Loss of mitochondrial proteins leads to generation of elongated paraspeckles. a, Probes used for *NEAT1* FISH. **b**, Representative images from two independent experiments of paraspeckles in shRNA-treated HeLa cells under SIM. Scale bar, 500 nm. See also Supplementary Fig. 2c. **c**, Left, Statistics of paraspeckle number ($n = 164, 123, 60, 60, 94, 97, 148, 57$ cells randomly selected under each condition). Right, Bar graph showing distribution of different paraspeckles. Paraspeckles were classified into three categories as described in ref. [12]. Data collected from two independent FISH experiments in **b**. **d**, Representative images from three independent experiments of paraspeckles in shRNA-treated HEK293 cells under SIM. Scale bar, 500 nm. See also Supplementary Fig. 2f. Bar graph (top right) shows the distribution of different paraspeckles. **e**, Knockdown nuclear-encoded mitochondrial proteins reduced *atf2* expression, shown by RT–qPCR ($n = 3$ independent experiments). **f**, Knockdown BCL2 impaired ATF2 expression, whereas ATF2 disruption had no effect on BCL2, shown by western blot. Data represent two independent experiments. **g**, Knockdown nuclear-encoded mitochondrial proteins reduced ATF2 expression, shown by western blot. Data represent two independent experiments. **h**, ATF2 knockdown had little effect on the expression of nuclear-encoded mitochondrial proteins revealed by RT–qPCR. Data represent two independent experiments. Data in **c**, **e** and **h** are presented as mean ± s.d. All *P* values are calculated using two-tailed unpaired Student's *t*-test; **$P < 0.01$, ***$P < 0.001$. Statistical source data, including precise *P* values, are provided in Supplementary Table 6. Unprocessed blots for **f** and **g** are provided in Supplementary Fig. 8.
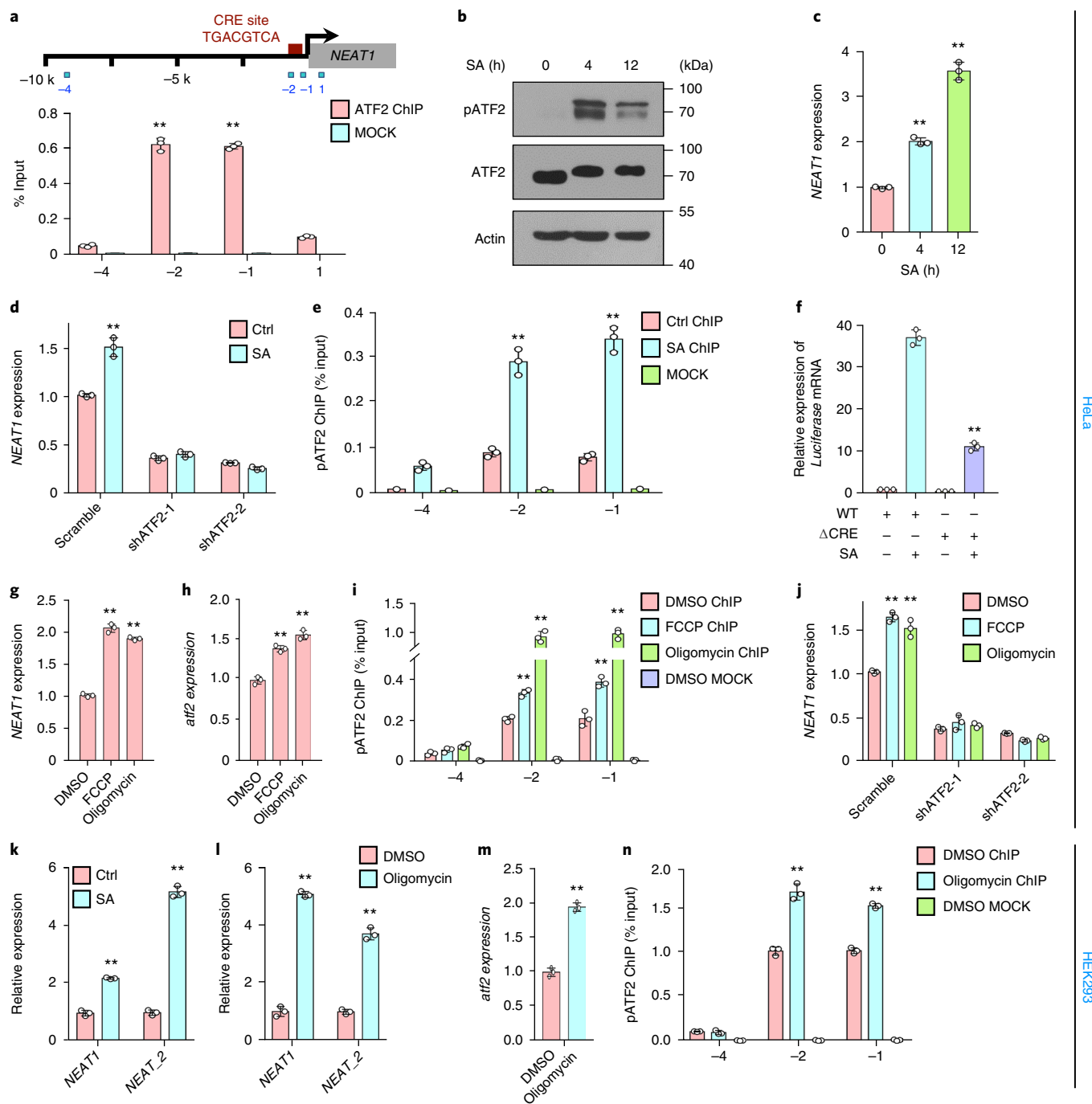
Fig. 3 | Mitochondrial signals regulate *NEAT1* expression via ATF2. a, Top, ATF2 binding site (CRE) and primers used in ATF2 ChIP. Bottom, ATF2 is enriched on *NEAT1* promoter (*n* = 3 independent experiments). **b**, Western blot showing SA (500 μM, 4 h) treatment elevated Thr71 phosphorylation of ATF2 in HeLa cells. Data represent two independent experiments. **c**, SA-treatment-induced *NEAT1* expression, shown by RT–qPCR (*n* = 3 independent experiments). **d**, SA-treatment-induced *NEAT1* expression depended on ATF2, as shown by RT–qPCR (*n* = 3 independent experiments). **e**, Phosphorylated ATF2 bound to the *NEAT1* promoter following SA treatment. Numbers shown on the *x* axis correspond to primers indicated in **a** (*n* = 3 independent experiments). **f**, Cells were transfected with *NEAT1* promoter-luciferase constructs (WT or ΔCRE) and pmCherry-C1 (control) followed by SA treatment. *Luciferase* expression was normalized to *mCherry* (*n* = 3 independent experiments). **g,h**, Mitochondrial stressors FCCP (2 μM, 24 h) and oligomycin (2 μM, 24 h) induced *NEAT1* (**g**) and *atf2* (**h**) expression, as shown by RT–qPCR. DMSO was used as control (*n* = 3 independent experiments). **i**, Phosphorylated ATF2 bound to *NEAT1* promoter following FCCP and oligomycin (2 μM, 24 h) treatments. Numbers shown on the *x* axis correspond to primers indicated in **a** (*n* = 3 independent experiments). **j**, FCCP and oligomycin-induced *NEAT1* expression depended on ATF2, as shown by RT–qPCR (*n* = 3 independent experiments). **k,l**, RT–qPCR revealed that SA (500 μM, 12 h) (**k**) and oligomycin (2 μM, 24 h) (**l**) induced *NEAT1* expression in HEK293 cells (*n* = 3 independent experiments). **m**, RT–qPCR revealed that oligomycin-induced *atf2* expression in HEK293 cells (*n* = 3 independent experiments). **n**, Phosphorylated ATF2 bound to *NEAT1* promoter following oligomycin treatment in HEK293 cells (*n* = 3 independent experiments). Data in **a**, **c–n** are presented as mean ± s.d. All *P* values were calculated using two-tailed unpaired Student's *t*-test; **P < 0.01. Statistical source data, including precise *P* values, are provided in Supplementary Table 6. Unprocessed blots for **b** are shown in Supplementary Fig. 8.

SA could activate ATF2 by enhancing its phosphorylation (Fig. 3b) and robustly induce *NEAT1* expression (Fig. 3c). Importantly, this induction depended on ATF2 (Fig. 3d), and enrichment of phosphorylated ATF2 at the *NEAT1* promoter was increased on SA treatment (Fig. 3e). Finally, the CRE site was essential for SA-induced activation of the *NEAT1* promoter, as shown by assays using WT or CRE-deleted *NEAT1* luciferase reporters (Fig. 3f).

Similarly, other mitochondrial stressors (mito-stressors) such as carbonyl cyanide 4-(trifluoromethoxy)phenylhydrazone (FCCP), oligomycin (Fig. 3g), rotenone and doxycycline (Supplementary Fig. 3f) all led to increased *NEAT1* transcription. FCCP and oligomycin also induced ATF2 expression (Fig. 3h). Further analyses on FCCP and oligomycin showed that enrichment of phosphorylated ATF2 at the *NEAT1* promoter increased following these treatments (Fig. 3i) and that such *NEAT1* upregulations were no longer detected in ATF2-depleted cells (Fig. 3j). Finally, increased *NEAT1* transcription induced by different mito-stressors was also detected in other types of cell (Fig. 3k-n and Supplementary Fig. 3g-i).

Together, these results show that ATF2 directly binds to the *NEAT1* promoter to enhance *NEAT1* transcription in response to mitochondrial defects involving loss of mitochondrial proteins and mito-stressor treatments.

Increased production of *NEAT1_2* promotes formation of elongated paraspeckles. The majority of paraspeckles were globular under normal conditions (Fig. 2b,c)[12], so it was interesting to observe the formation of elongated paraspeckles in response to mitochondrial defects (Fig. 2b-d and Supplementary Fig. 2). It has been shown that increasing *NEAT1_2* levels could promote the generation of elongated paraspeckles in cells by proteasome inhibition[14], so we asked whether *NEAT1* transcription in response to mitochondrial defects might lead to altered processing of *NEAT1_1* and *NEAT1_2* for elongated paraspeckle formation. RT–PCR revealed that the percentage of *NEAT1_2* was augmented in cells depleted of the examined mitochondrial proteins (Fig. 4a and Supplementary Fig. 3a,b), even though overall levels of *NEAT1* expression were reduced to about 50% (Fig. 1g,h). Similar observations were confirmed by RNase protection assays following BCL2 knockdown (Fig. 4b).

To further confirm that the defect in *NEAT1* processing of its two isoforms, rather than the abundance of total *NEAT1*, is the direct cause of elongated paraspeckle formation, we used CRISPR/Cas9 to disrupt the 3′-end poly(A) site of *NEAT1_1* (Fig. 4c) for favourable *NEAT1_2* production. Two individual clones with desired double-allele deletions at *NEAT1* (*NEAT1_1* Δp(A)) were selected, both of which exhibited increased *NEAT1_2* expression to twofold, while the total *NEAT1* level remained unchanged (Fig. 4c). As expected, SIM observations of *NEAT1_1* Δp(A) cells revealed an obvious increase in elongated paraspeckles (Fig. 4d,e and Supplementary Fig. 3j), confirming that increased *NEAT1_2* promotes the generation of elongated paraspeckles.

Elongated paraspeckles have reduced dynamic behaviour of NONO and increased capability of mRNA sequestration. Next, we asked whether elongated paraspeckles have any functional difference compared to normal, globular bodies. NONO is one of the paraspeckle structural protein components and is localized in the core region of paraspeckles[5,12]. NONO binds to mRNAs with IR*Alu*s in their 3′ UTRs and contributes to their nuclear retention within paraspeckles[1,6,18–21]. Thus, the characteristics of NONO in these two types of morphologically distinct paraspeckle may indicate their functional difference, if any.

Cells under BCL2 knockdown or *NEAT1_1* Δp(A) conditions show a remarkable increase in elongated paraspeckles (Figs. 2c and 4e). We examined the kinetics of NONO by fluorescence recovery after photobleaching (FRAP) within individual globular or elongated paraspeckles in these cells. Transfection of EGFP-NONO was found to be richly localized to both types of paraspeckle, without a noticeable difference under prebleach condition (Fig. 4f). We observed an exchange rate of NONO in globular paraspeckles with $t_{1/2} = 27–31$ s (Fig. 4f,g), which is comparable to other paraspeckle proteins (such as GFP-PSP1) examined in HeLa cells[38]. However, the recovery of NONO was strikingly delayed in elongated paraspeckles compared to globular paraspeckles in cells under BCL2 depletion or altered *NEAT1* processing (Fig. 4f,g). Their $t_{1/2}$ could not be accurately measured because NONO recovery in elongated paraspeckles never reached a plateau, but a reasonable estimation suggests $t_{1/2} > 45–50$ s. These analyses indicate a distinct effect of paraspeckle proteins in elongated and globular paraspeckles.

The reduced exchange of NONO within elongated paraspeckles would suggest an increased interaction between NONO and *NEAT1* and hence an augmented capability of mRNA paraspeckle retention. To test this possibility, we performed NONO immunoprecipitation assays followed by detection of *NEAT1* and previously known paraspeckle-retained IR*Alu*s-mRNAs by this protein[6,19–21] in cells having increased elongated paraspeckles. As expected, we observed that more RNAs were associated with NONO in BCL2 knockdown or *NEAT1_1* Δp(A) cells than in normal cells (Fig. 4h,i).
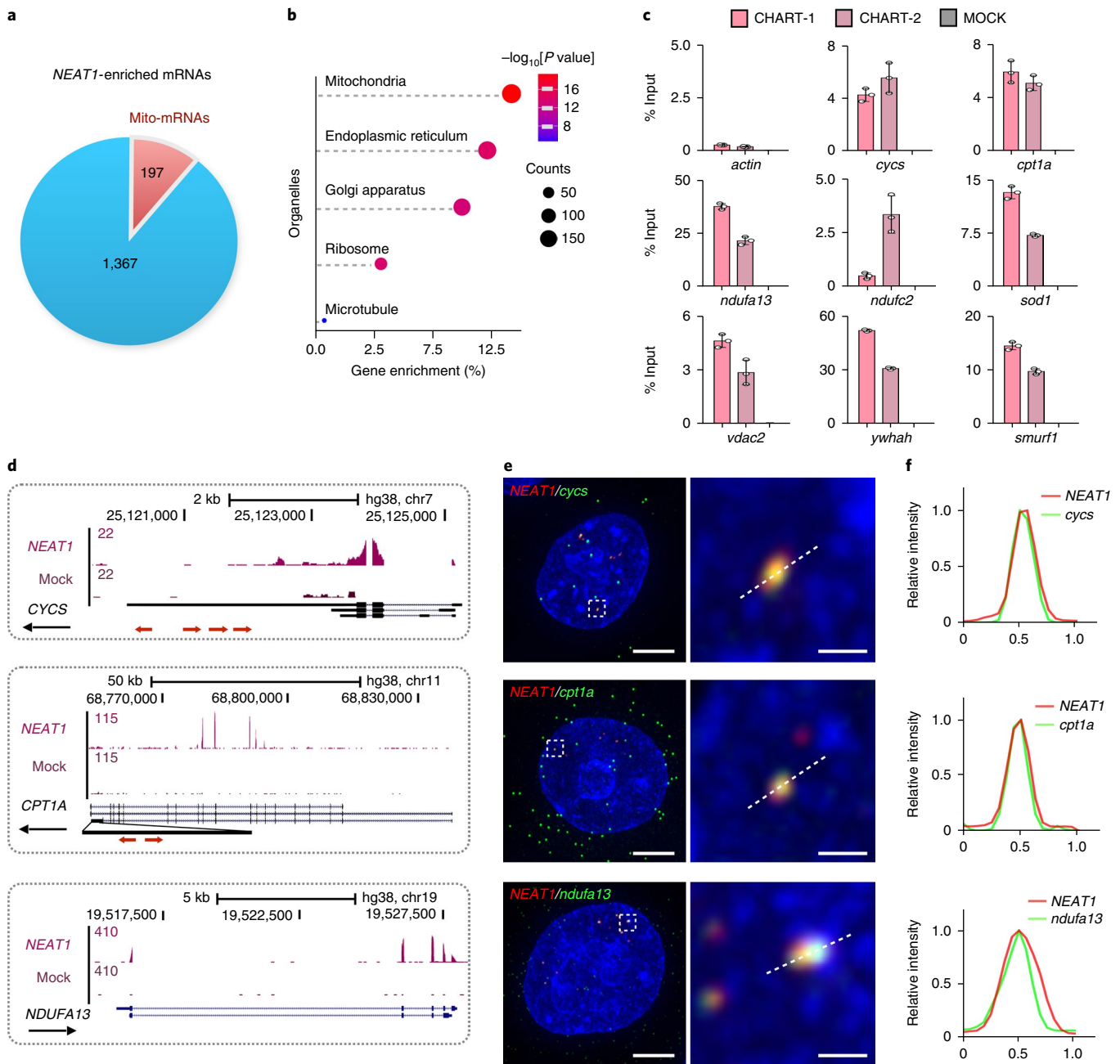
Together, these results suggest that elongated paraspeckles formed in response to mitochondrial protein depletion are functionally different from the regular, globular bodies.

Sequestration of mRNAs of nuclear-encoded mitochondrial proteins by *NEAT1* and paraspeckles. Why might it be important to have elongated paraspeckles in response to loss of mitochondrial proteins? As a global inspection of RNAs trapped by paraspeckles in human cells has been lacking, we performed CHART (capture hybridization analysis of RNA targets) assays with antisense probes recognizing both *NEAT1* isoforms at the 5′ ends followed by RNA–seq in HeLa cells (Supplementary Fig. 4a,b). A total of 197 nuclear-encoded mitochondrial proteins (mito-mRNAs) were potentially associated with paraspeckles (Fig. 5a), and were over-presented compared to the CHART-enriched mRNAs of nuclear genes that encode other reported cellular functions (Fig. 5b). Among these CHART-enriched mito-mRNAs, 15 mRNAs contain IR*Alu*s in their 3′ UTRs, the known *cis*-elements for paraspeckle-mediated retention.

Additional mRNAs with AG- or U-rich motifs were also found to be associated with *NEAT1* paraspeckles (Supplementary Fig. 4c), consistent with a study performed in mice[12]. Selected mito-mRNAs enriched by *NEAT1* with or without IR*Alu*s could be validated by independent CHART assays (Fig. 5c). These mito-mRNAs include *CYCS*, which encodes cytochrome *c*, a key player in mitochondrial-mediated apoptosis[39,40]; *NDUFA13*, which encodes a subunit of mitochondrial membrane respiratory chain NADH dehydrogenases[41]; and *CPT1A*, which encodes an integral outer membrane protein that converts activated fatty acids into acylcarnitines[42,43] (Fig. 5d). Representative examples are shown in Supplementary Fig. 4d. Importantly, their paraspeckle localizations were confirmed using dual-colour single-molecule RNA FISH (smFISH) with probes only targeting the *NEAT1_2* isoform and individual *NEAT1*-enriched mito-mRNAs in single cells (Fig. 5e,f). Finally, generation of network maps of these retained mRNAs revealed that their encoded proteins are involved in mitochondrial functions and diseases (Supplementary Fig. 4e).

Enhanced nuclear retention of mito-mRNAs in paraspeckles in response to mitochondrial defects. Paraspeckle-retained mito-mRNAs with or without 3′ UTR IR*Alu*s were associated with NONO, and exhibited an augmented interaction with this protein in cells that have elongated paraspeckles in response to depletion of BCL2 (Fig. 6a) or *NEAT1_1* poly(A) site (Fig. 6b). At the single cell level, three examined mito-mRNAs—*cycs* and *cpt1a*, whose

Fig. 4 | Increased production of *NEAT1_2* promotes the formation of elongated paraspeckles and the capability of mRNA sequestration. a, Relative ratio of *NEAT1_2* to total *NEAT1* in mitochondrial-protein-depleted cells, detected by RT–qPCR ($n = 3$ independent experiments). **b**, Top, Schematic drawing showing the probe used in the RNase protection assay (RPA). Bottom, Increased proportion of *NEAT1_2* following BCL2 knockdown revealed by RPA. Data shown represent three independent experiments. **c**, Top, Schematic drawing shows the polyadenylation site p(A) of *NEAT1_1* and sgRNAs used to delete the poly(A) site to increase the proportion of *NEAT1_2*. Bottom, Poly(A) site deletion results in increased *NEAT1_2* accumulation in two Δp(A) clones, shown by RT–qPCR using primer sets indicated in blue on the top ($n = 3$ independent experiments). **d**, Representative images of SIM observations of paraspeckles in two Δp(A) clones. Scale bars, 500 nm. Data represent two independent experiments. **e**, Bar graph showing the distribution of different paraspeckles from two independent FISH experiments. **f,g**, Representative fluorescent recovery after photobleaching (FRAP) images (**f**) of the EGFP-NONO and kinetics (**g**) of NONO recovery in BCL2 knockdown (KD) cells (top, $n = 13$ and 27 for globular and elongated paraspeckles, respectively) or *NEAT1_1* Δp(A) cells (bottom, $n = 18$ and 21 for globular and elongated paraspeckles, respectively). Data are from two independent FRAP experiments. Scale bars, 2 μm. **h,i**, Enhanced association of NONO with *NEAT1* (top) and IR*Alus*-mRNAs[1,20,21] (bottom) in BCL2 knockdown (**h**) and Δp(A) (**i**) cells. Bar graphs represent fold enrichments of RNAs immunoprecipitated by anti-NONO or anti-mouse IgG2b over the same amount of input from equal amounts of cells across different samples. 18S rRNA was a control ($n = 3$ independent experiments). Data in **g** are presented as mean ± s.e.m. and in **a**, **c**, **h**, **i** as mean ± s.d. All *P* values calculated using two-tailed unpaired Student's *t*-test; *$P < 0.05$, **$P < 0.01$. Statistical source data, including precise *P* values, are provided in Supplementary Table 6. Unprocessed blots for **b** are shown in Supplementary Fig. 8.

Fig. 5 | Sequestration of mito-mRNAs by *NEAT1* and paraspeckles. a, Venn diagram showing *NEAT1*-enriched RNAs by CHART, using the *NEAT1* antisense probes shown in Supplementary Fig. 4a. See also Supplementary Fig. 4b,c. **b**, Bubble plot presenting one *NEAT1* CHART–RNA–seq of enriched mRNAs encoding proteins related to different cellular organelles. The *x* axis shows the ratio of the number of enriched mRNAs in each different organelle divided by the number of total *NEAT1*-enriched RNAs (one-sided Fisher's exact test). The *y* axis shows the category of organelles. See also Supplementary Fig. 4e. **c**, Validation of mito-mRNAs with or without IR*Alu*s enriched by *NEAT1* CHART–RNA–seq. Data from three independent CHART experiments represent mean ± s.d. **d**, Representative wiggle tracks of the *NEAT1*-enriched mito-mRNAs in one RNA–seq from three independent CHART experiments. Red arrows indicate location of inverted repeat *Alu* (IR*Alu*). The 3′ UTR region of *CPT1A* is magnified to indicate the positions of IR*Alu*s. See also Supplementary Fig. 4d. **e**, Validation of mito-mRNAs enriched by *NEAT1* CHART–RNA-seq including *cycs*, *cpt1a* and *ndufa13* by smFISH. Scale bars, 5 μm (uncropped) and 500 nm (cropped). Data represent three independent smFISH experiments. **f**, Line graphs of both fluorescence intensities in **e** showing co-localization along the entire length of each dashed line. Data represent three independent experiments with similar results. Statistical source data are provided in Supplementary Table 6.

3′ UTRs contain IR*Alu*s, as well as *ndufa13*, which does not have IR*Alu*s—all exhibited remarkably increased co-localization signals with *NEAT1* in elongated paraspeckles in BCL2-depleted cells (Fig. 6c,d and Supplementary Fig. 5a–c).

We next examined whether the nuclear retention of mito-mRNAs within paraspeckles was altered in cells treated with

mito-stressors. First, previously reported paraspeckle-localized mRNAs (Fig. 4h,i) and newly identified mito-mRNAs all exhibited increased association with NONO in cells treated with FCCP (Fig. 6e and Supplementary Fig. 5d,e). SIM images of paraspeckles in cells treated with FCCP showed no apparent morphological changes (Supplementary Fig. 5f), but exhibited increased numbers
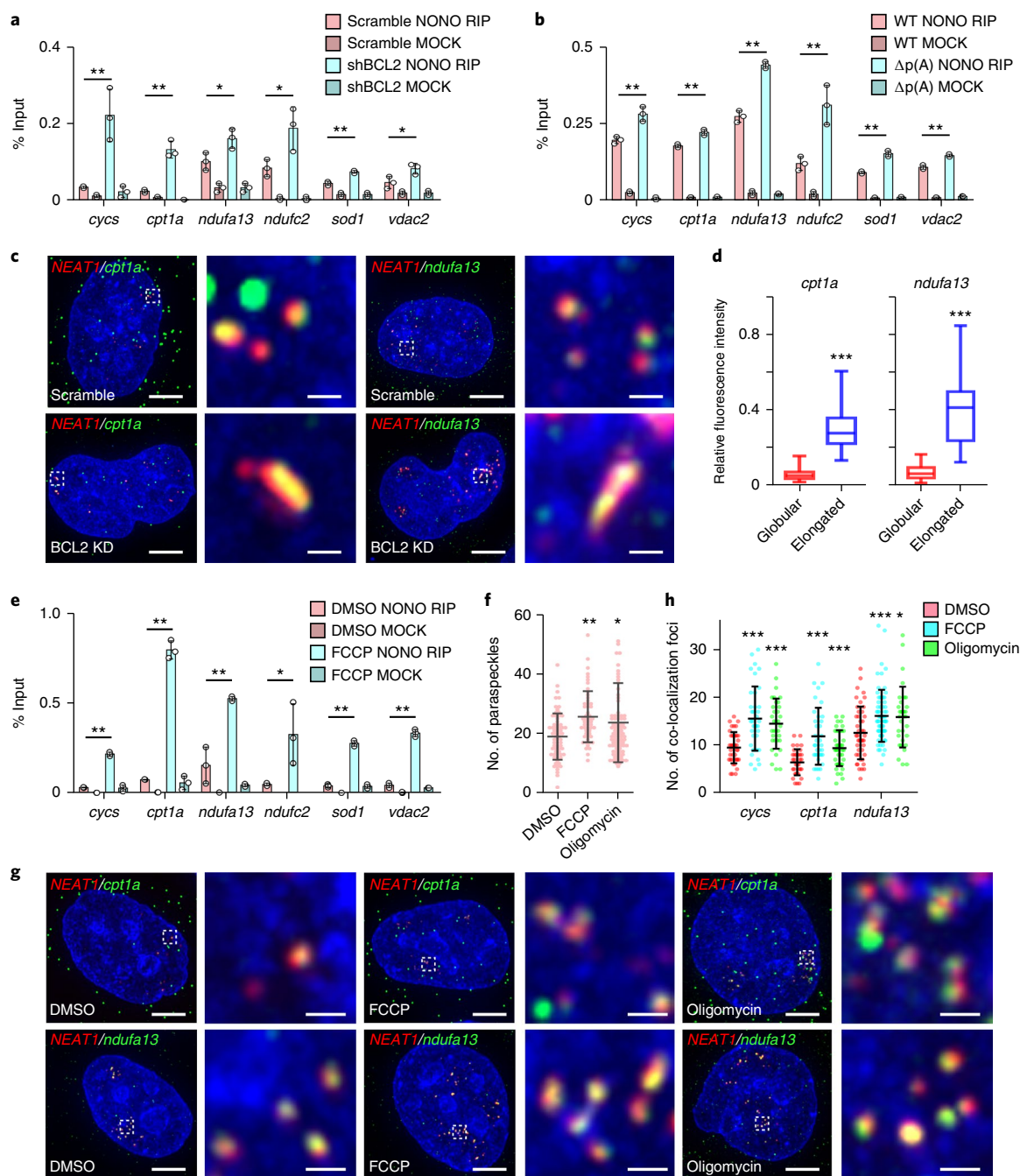
Fig. 6 | Enhanced nuclear retention of mito-RNAs in paraspeckles in response to mitochondrial detects. a,b, Enhanced association of NONO with *NEAT1*-enriched mito-mRNAs, as revealed by native NONO immunoprecipitation in BCL2 knockdown (**a**) or Δp(A) cells (**b**) (*n* = 3 independent experiments). **c**, Representative pictures of the co-localization of *NEAT1* and two CHART-enriched mito-mRNAs by smFISH. Scale bars, 5 µm (uncropped) and 500 nm (cropped). See also Supplementary Fig. 5a,b. Data represent three independent experiments. **d**, Relative fluorescence intensity of mito-mRNAs in globular and elongated paraspeckles. See also Supplementary Fig. 5c (*n* = 50 for each type of paraspeckle, which were randomly selected from three independent smFISH experiments). **e**, Enhanced association of NONO with *NEAT1*-enriched mito-mRNAs, as revealed by native NONO immunoprecipitation in FCCP (2 µM, 24 h) treated cells, compared to DMSO (control) treated cells. See also Supplementary Fig. 5d,e. (*n* = 3 independent experiments.) **f**, Statistics of paraspeckle number per cell following DMSO, FCCP (2 µM, 24 h) and oligomycin (2 µM, 24 h) treatments. *n* = 67, 53, 88 cells randomly collected from three independent FISH experiments. **g**, Representative images of the co-localization of *NEAT1* and two CHART-enriched mito-mRNAs by smFISH in cells upon DMSO, FCCP (2 µM, 24 h) or oligomycin (2 µM, 24 h) treatments. Scale bars, 5 µm (uncropped) and 500 nm (cropped). See also Supplementary Fig. 5h. Data represent three independent experiments. **h**, Numbers of co-localized foci between *NEAT1* and *NEAT1* CHART-enriched mito-RNAs following FCCP and oligomycin (2 µM, 24 h) treatments using smFISH (*n* = 40, 37, 34, 34, 36, 40, 45, 67, 32 cells randomly collected separately from three independent smFISH experiments). Data in **a**, **b**, **e**, **f** and **h** are presented as mean ± s.d. Box and whisker plot in **d** are shown with centre line at median, box limits at 25th/75th centiles and whiskers from minimum to maximum. All *P* values are calculated using two-tailed unpaired Student's *t*-test; *P < 0.05, **P < 0.01, ***P < 0.001. Statistical source data, including precise *P* values, are provided in Supplementary Table 6.

of globular paraspeckles (Fig. 6f). These SIM observations are consistent with the notion that total *NEAT1* levels increased with an unchanged ratio of the two *NEAT1* isoforms (Supplementary Fig. 5g). Correspondingly, *NEAT1*-co-localized mito-mRNAs (*cycs*, *capt1a* and *ndufa13*) were increased in cells with increased numbers of paraspeckles following FCCP and oligomycin treatments (Fig. 6g,h and Supplementary Fig. 5h). As a control, the subcellular distribution of *actin* mRNA was not changed under the same treatments (Supplementary Fig. 5i).

Collectively, these findings suggest a communication between paraspeckles and mitochondria. Paraspeckle function and mitochondrial signals are coupled by controlling *NEAT1* transcription and processing, which are associated with increased numbers of globular paraspeckles or formation of elongated paraspeckles in response to mito-stressors or loss of mitochondrial proteins. Cells under these conditions show enhanced capability to trap mito-mRNAs in the nucleus, which can act as one way to quickly perturb mito-mRNAs exporting to the cytoplasm for translation.

***NEAT1* and paraspeckles are essential for mitochondrial homeostasis.** Communication between mitochondria and the nucleus is tightly coordinated during homeostasis and mitochondrial stress[27]. The observed changes of paraspeckle dynamics and function in response to mitochondrial protein depletion and different mito-stressors (Figs. 2–6) indicated a previously unknown view that paraspeckles may regulate mitochondrial homeostasis. To test this hypothesis, we knocked out (KO) *NEAT1* in HeLa cells (Supplementary Fig. 6a,b), then examined a number of factors that indicate mitochondrial features.

Strikingly, *NEAT1*-depleted single cell clones showed a consistent reduction in mitochondrial DNA (mtDNA) (Fig. 7a), reduced mitochondrial respiration (by detection of the oxygen consumption rate (OCR); Fig. 7b) and adenosine triphosphate (ATP) production (Fig. 7c), reduced OCR and extracellular acidification rate (ECAR) rate (Fig. 7d), suggesting that the aberrant *NEAT1* expression could cause mitochondrial dysfunction. Furthermore, in agreement with the impaired mitochondrial function (Fig. 7a-d), *NEAT1* knockout cells showed reduced proliferation rate (Fig. 7e). In addition, *NEAT1*-depleted single cell clones tended to have elongated mitochondria (Fig. 7f and Supplementary Fig. 6c). The fission and fusion of mitochondria (collectively termed mitochondrial dynamics) work in concert to maintain the normal morphology, number and health of mitochondria[44]. Mitochondrial dynamics is regulated by a group of highly conserved large dynamin-related GTPase proteins (DRPs), including MFN1 and MFN2 (required for fusion) and DRP1 (responsible for fission)[44]. We found that DRP1 expression, as well as phosphorylated DRP1, were both decreased in *NEAT1* knockout cells, whereas MFN1 and MFN2 expression remained unchanged (Fig. 7g), indicating that a defect of mitochondrial fission contributed to elongated mitochondria in *NEAT1*-depleted cells. Similar impaired mitochondrial function and dynamics were observed in antisense oligonucleotide (ASO)-mediated *NEAT1* knockdown in HeLa (Supplementary Fig. 6d-i) and HEK293 cells (Supplementary Fig. 6j-n).

Finally, consistent with observed mitochondrial defects in cells without *NEAT1*, HeLa cells with *NEAT1 in cis* induction by dCas9-VP64 and specific sgRNAs (Supplementary Fig. 6a) to activate *NEAT1* transcription (Fig. 7h) showed increased mtDNA (Fig. 7i), more fragmented mitochondria (Fig. 7j), increased DRP1 expression and phosphorylation (Fig. 7g) than those in empty sgRNA vector treated cells. In addition, *NEAT1_1* Δp(A) cells with increased elongated paraspeckles (Fig. 4d,e) exhibited similar changes in mitochondrial defects (Fig. 7k-m), DRP1 expression and phosphorylation (Fig. 7g) as those in *NEAT1* upregulated cells. These results together support a critical role of *NEAT1* and paraspeckles in the regulation of mitochondrial homeostasis.

Sequestration of mito-mRNAs within paraspeckles is involved in mito-paraspeckle communication. Consistent with aberrant mitochondrial homeostasis, paraspeckle-enriched mito-mRNAs exhibited enhanced nucleocytoplasmic export in *NEAT1* knockout cells (Fig. 8a). In contrast, genome-wide RNA–seq of two *NEAT1* knockout clones and their control cells revealed little change on the transcription of genes encoding mitochondrial proteins (Supplementary Fig. 7a-d), indicating that hundreds of mRNAs coding for mitochondrial proteins being enriched in paraspeckles (Fig. 5) probably plays a role in coordinating the crosstalk between these two subcellular compartments.

To further illustrate this notion, we focused on *CYCS* that encodes cytochrome *c*. It is well known that the release of cytochrome *c* from mitochondria induces the mitochondrial pathway of apoptosis[40]. Prolonged treatment with the mitochondrial stressor SA led to cytochrome *c* release from mitochondria to cytosol (Fig. 8b) and severe cell death (Fig. 8c and Supplementary Fig. 7e-g). In the meantime, the cytochrome *c* protein level being translated in the cytoplasm was reduced (Fig. 8d and Supplementary Fig. 7h) although the total *cycs* mRNA remained unchanged (Fig. 8e). Correspondingly, paraspeckles-retained *cycs* increased in cells treated with SA (Fig. 8f). Thus, *cycs* mRNA nuclear retention represents a quality control mechanism to prohibit unnecessary cytochrome *c* from being translated following stress. Importantly, cells lacking *NEAT1* exhibited significantly greater cell apoptosis than WT cells following SA induction (Fig. 8c and Supplementary Fig. 7e-g). In keeping with this observation, the cytochrome *c* protein level was much higher on SA induction than that in WT cells (Fig. 8d and Supplementary Fig. 7h) due to the increased nuclear export of *cycs* mRNAs in cells without paraspeckles (Fig. 8a).

Thus, *NEAT1* and paraspeckles can regulate mitochondrial homeostasis, at least partially, through the nuclear retention of multiple mitochondria-related mRNAs. Such a paraspeckle-mediated mRNA nuclear retention pathway can act as a quality control mechanism to sequester or release mRNAs depending on cellular needs.

Discussion

lncRNAs are emerging as regulators of the gene expression network through various modes of action[45,46]. How the lncRNA genes contribute to communication with other cell components remains poorly understood. Using endogenous *NEAT1*-promoter-driven EGFP expression as a readout for genome-wide screening of *NEAT1* regulators (Fig. 1), we uncovered a feedback loop of mitochondrial stress-*NEAT1*/paraspeckles-mitochondrial homeostasis (Fig. 8g). The increase in elongated paraspeckles and augmented capability for mRNA sequestration in the nucleus following the loss of mitochondrial proteins suggests a previously under-estimated regulation on *NEAT1* transcription and paraspeckle function (Figs. 2–6). Formation of elongated paraspeckles requires an increased proportion of the long isoform in relation to the short *NEAT1* isoform (Fig. 4 and Supplementary Fig. 3j)[14], although how this transition occurs remains to be studied (Supplementary Fig. 7i). One possibility is that ATF2 itself might modulate 3′-end processing of *NEAT1_1*, in addition to its role in *NEAT1* transcription (Figs. 2 and 3 and Supplementary Fig. 7i).

Several key paraspeckle protein components are RNA binding proteins[12] that harbour intrinsically disordered regions that can drive liquid–liquid phase separation[47–49]. Examined proteins within paraspeckles exhibit dynamic exchange with the nucleoplasm[6,38] (Fig. 5), suggesting that paraspeckles represent a type of membrane-less liquid-like nuclear body. We found suppressed mobility of NONO and increased mito-mRNA sequestration in elongated paraspeckles (Figs. 4 and 6), supporting the view that elongated paraspeckles behave in a more condensed state. It remains to be determined how elongated paraspeckles are assembled and whether they are reversible to the globular form. It is possible that an elongated paraspeckle
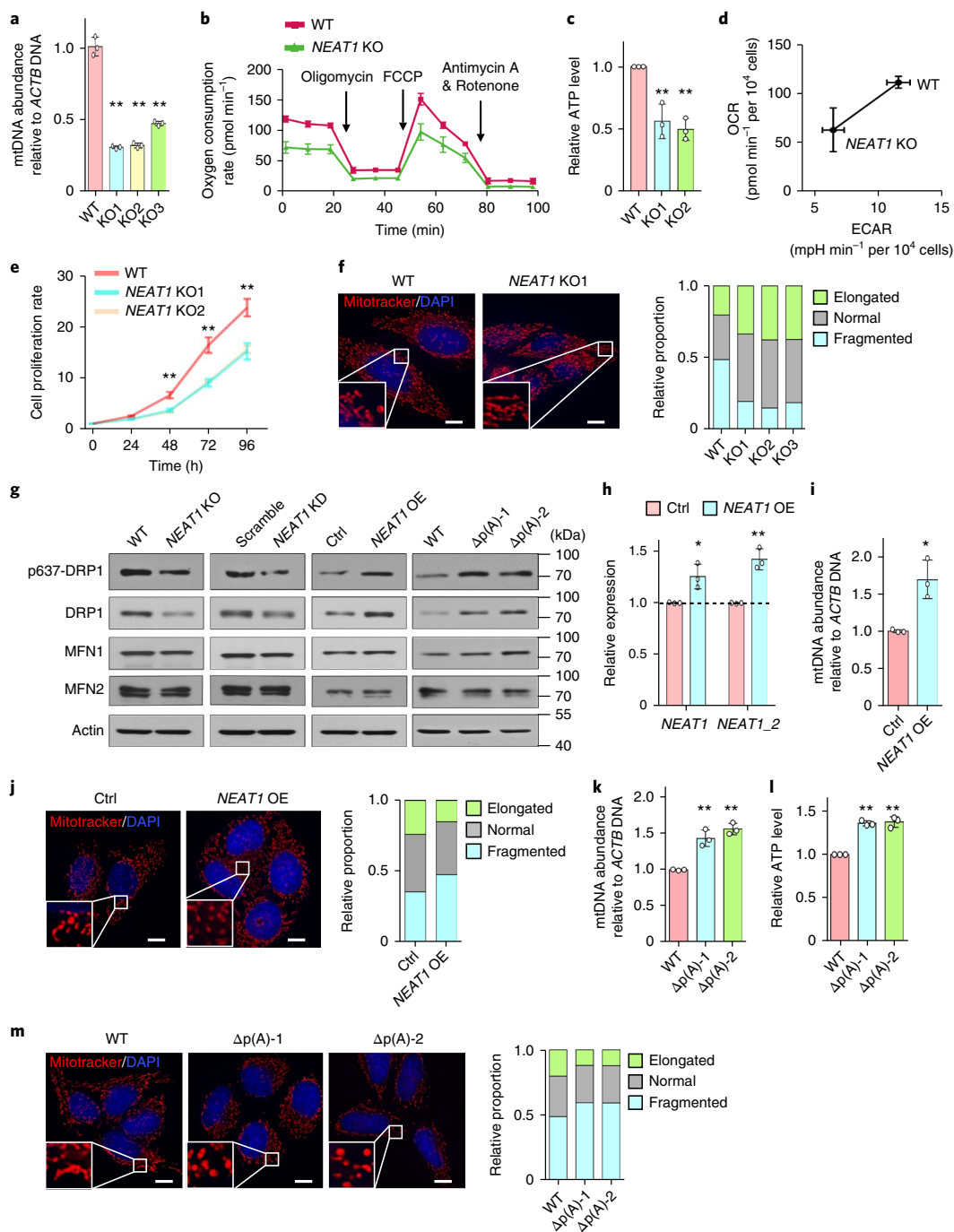
Fig. 7 | Altered *NEAT1* expression leads to mitochondria defects. a, *NEAT1* deletion led to reduced mtDNA, shown by qPCR of mtDNA normalized to *ACTB* gDNA (*n* = 3 independent experiments). **b**, *NEAT1* deletion impaired mitochondrial respiration, detected by Seahorse assays (*n* = 3 independent experiments). **c**, *NEAT1* deletion reduced ATP production, detected by ATP viability assays (*n* = 3 independent experiments). **d**, OCR and ECAR in control and *NEAT1* knockout (KO) HeLa cells (*n* = 3 independent experiments). **e**, *NEAT1* KO cells have reduced proliferation rates, detected by the 3-(4,5-dimethylthiazol-2-yl)-2,5-diphenyltetrazolium bromide (MTT) assay (*n* = 3 independent experiments). **f**, Left, Mitochondria labelled by Mitotracker-red under DeltaVision microscopy showed mitochondria hyper-fusion upon *NEAT1* deletion. Scale bar, 10 μm. Right, Bar graph showing three categories of mitochondria[51]: elongated (radius$_{max}$/radius$_{min}$ > 7), normal (~2–7), and fragmented (~1–2). See Methods for details. Data represent three independent experiments. **g**, Expression of DRP1, p637-DRP1, MFN1, MFN2 in *NEAT1* KO, KD, overexpression (OE) or *NEAT1_1* Δp(A) cells, shown by western blot. Data represent four independent experiments. Three *NEAT1* KO or KD clones were mixed for western blot. **h**, *NEAT1* OE by dCas9 in HeLa cells was confirmed by RT–qPCR (*n* = 3 independent experiments). **i**, qPCR showed increased mtDNA abundance in *NEAT1* OE cells (*n* = 3 independent experiments). **j**, Left, Morphological changes of mitochondria in *NEAT1* OE cells. Scale bar, 10 μm. Right, Bar graph showing each category of mitochondria. Data represent three independent experiments. **k**, qPCR showed increased mtDNA in *NEAT1_1* Δp(A) cells (*n* = 3 independent experiments). **l**, ATP viability assay showed enhanced ATP production in *NEAT1_1* Δp(A) cells (*n* = 3 independent experiments). **m**, Left, Morphological changes of mitochondria in *NEAT1_1* Δp(A) cells. Scale bars, 10 μm. Right, Bar graph showing each category of mitochondria. Data represent three independent experiments. Data in **a**–**e**, **h**, **i**, **k** and **l** presented as mean ± s.d. All *P* values calculated using two-tailed unpaired Student's *t*-test; *P < 0.05, **P < 0.01. Statistical source data, including precise *P* values, are provided in Supplementary Table 6. Unprocessed blots for **g** are shown in Supplementary Fig. 8.
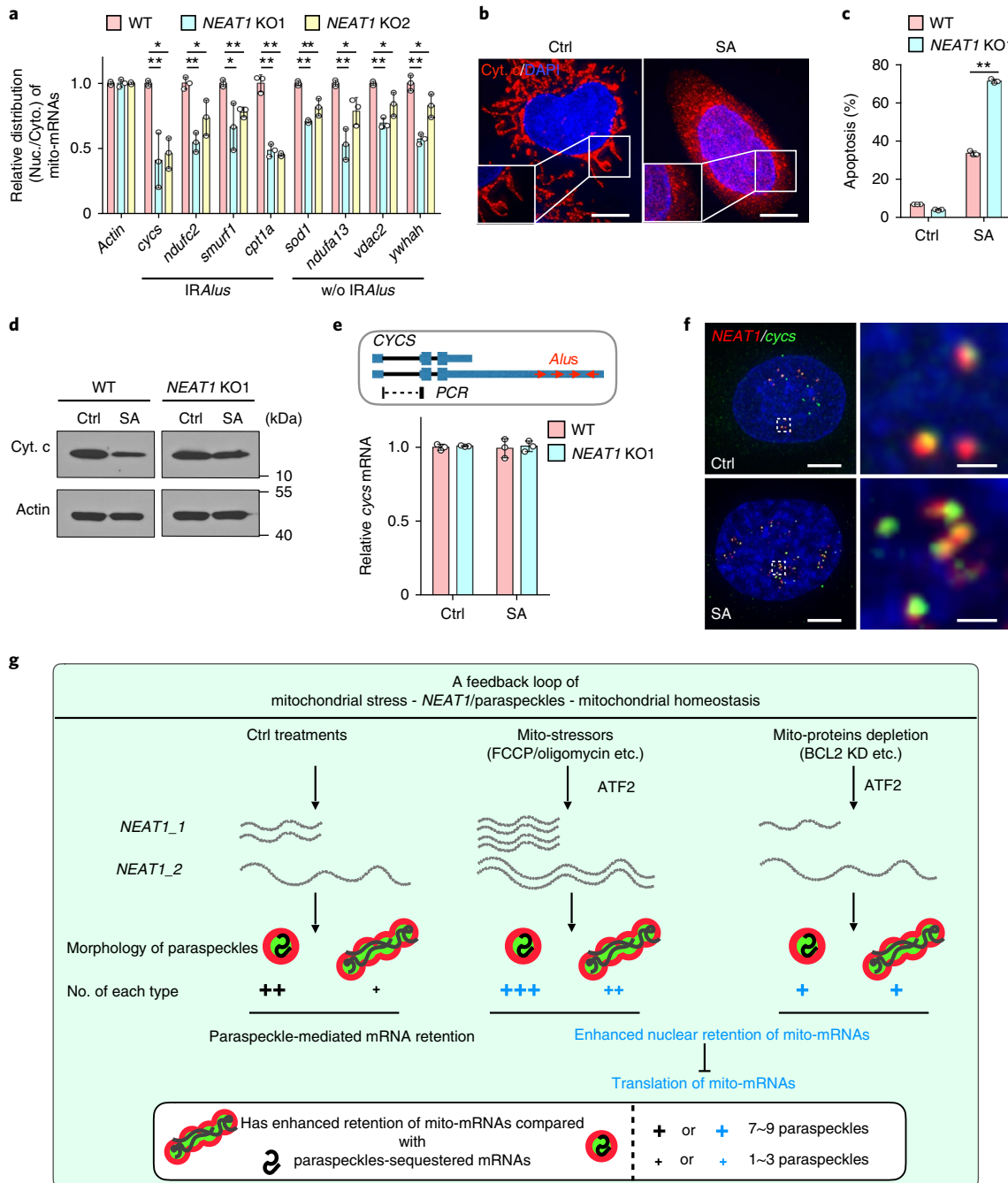
Fig. 8 | NEAT1 protects cells from apoptosis induced by mitochondrial stressor SA and a proposed model of mito-paraspeckle communication. a, *NEAT1*-depleted HeLa cells have enhanced nucleocytoplasmic export of the examined mito-mRNAs. RT–qPCR examined mito-mRNAs enriched by *NEAT1* using nuclear and cytoplasmic fractionated RNAs. Of note, *actin* mRNA is not associated with *NEAT1*, nor has an altered cellular fate in response to *NEAT1* knockout (*n* = 3 independent experiments). **b,** SA treatment led to cytochrome c (Cyt. c) release from mitochondria to cytosol. Immunofluorescence of cytochrome *c* in control cells and cells treated with 500 μM SA for 24 h. Scale bars, 5 μm. Data represent three independent experiments. **c,** *NEAT1* knockout led to increased apoptosis induced by SA. WT or *NEAT1* knockout cells were treated with or without 500 μM SA for 24 h followed by annexin V staining and flow cytometry analyses of apoptosis. See also Supplementary Fig. 7e-g (*n* = 3 independent experiments). **d,** Cytochrome *c* expression following SA stimulation (500 μM, 24 h) in HeLa cells with or without *NEAT1*, detected by western blotting. See also Supplementary Fig. 7h. Data represent three independent experiments. **e,** Total *cycs* mRNA remained unchanged following SA treatment (500 μM, 24 h). Top, Schematic drawing showing two major isoforms of *cycs*. Arrows indicate *Alu* elements. Bottom, RT–qPCR reveals the expression of total *cycs* normalized to *actin*. Primers used are indicated at the top (*n* = 3 independent experiments). **f,** SA treatment led to increased sequestration of *cycs* mRNA in paraspeckles, as shown by smFISH. Scale bars, 5 μm (uncropped) and 500 nm (cropped). Data represent three independent experiments with similar results. **g,** Proposed model of cross-regulation between paraspeckles and mitochondria. See text for details. Data in **a**, **c** and **e** are presented as mean ± s.d. All *P* values calculated using two-tailed unpaired Student's *t*-test; *P < 0.05, **P < 0.01. Statistical source data, including precise *P* values, are provided in Supplementary Table 6. Unprocessed blots for **d** are shown in Supplementary Fig. 8.

is formed by the coalescence of two or more globular paraspeckles when the *NEAT1_2* isoform is increased following mitochondrial defects (Fig. 2). As the *NEAT1_2* middle domain is necessary and sufficient for paraspeckle assembly[50], it will be of interest to explore whether this domain is also required for elongated paraspeckle formation. Alternatively, new paraspeckles may be formed initially as elongated bodies; as soon as *NEAT1_1* is processed from its long isoform, the abundant short isoform may interact with different paraspeckle proteins to decondensate long paraspeckles, resulting in the production of round-shaped ones. Thus, the reduced level of *NEAT1_1* in response to mitochondrial protein depletion could ultimately result in an increased proportion of elongated paraspeckles (Fig. 4). Future development of new methods of imaging RNAs in live cells via super-resolution microscopy may determine the stepwise organization of paraspeckle morphogenesis.

The observed remarkable effects of paraspeckles on mitochondrial dynamics and function (Figs. 7 and 8) are achieved, at least in part, by trapping mito-mRNAs within paraspeckles (Figs. 5, 6 and 8). Given that mitochondria are one of the most important cellular organelles, we speculate that sequestration of many (rather than one) specific mito-mRNAs within paraspeckles accounts for the striking phenotypes of mitochondrial defects following altered *NEAT1* expression (Figs. 7 and 8). In addition, as many of these mito-genes, such as *CYCS*, which encodes cytochrome *c*, are essential for cellular growth under normal conditions, this paraspeckle-mediated mRNA sequestration offers a more flexible way of gene regulation than turning transcription of genes on or off (Figs. 6 and 8 and Supplementary Figs. 4, 5 and 7). How exactly mito-mRNAs trapped in paraspeckles can regulate different aspects of mitochondrial homeostasis remains to be explored. As *Neat1* knockout mice are viable under normal conditions[15,16], we speculate that the nuclear sequestration of mito-mRNAs by paraspeckles is unlikely to be critical in a non-stress scenario.

In summary, we have uncovered a cross-regulation between paraspeckles and mitochondria. Paraspeckles can sense mito-stressors via ATF2-mediated *NEAT1* transcription regulation, which in turn leads to changes in paraspeckle numbers and assembly, as well as mitochondrial dynamics and function. Such mito-paraspeckle communication represents one type of bidirectional signalling that is generated in reaction to mito-stressors to trigger particular nuclear paraspeckle responses. As a result, some mitochondrial mRNAs trapped by paraspeckles are altered in response to mitochondrial signals, leading to detectable changes in gene expression that may be needed to resolve perturbation in mitochondria through a mito-paraspeckle feedback (Fig. 8g).

Online content

Any methods, additional references, Nature Research reporting summaries, source data, statements of data availability and associated accession codes are available at https://doi.org/10.1038/s41556-018-0204-2.

References

1. Chen, L. L. & Carmichael, G. G. Altered nuclear retention of mRNAs containing inverted repeats in human embryonic stem cells: functional role of a nuclear noncoding RNA. *Mol. Cell* **35**, 467–478 (2009).
2. Clemson, C. M. et al. An architectural role for a nuclear noncoding RNA: NEAT1 RNA is essential for the structure of paraspeckles. *Mol. Cell* **33**, 717–726 (2009).
3. Sasaki, Y. T., Ideue, T., Sano, M., Mituyama, T. & Hirose, T. MENε/β noncoding RNAs are essential for structural integrity of nuclear paraspeckles. *Proc. Natl Acad. Sci. USA* **106**, 2525–2530 (2009).
4. Sunwoo, H. et al. MENε/β nuclear-retained non-coding RNAs are up-regulated upon muscle differentiation and are essential components of paraspeckles. *Genome Res.* **19**, 347–359 (2009).
5. Fox, A. H. et al. Paraspeckles: a novel nuclear domain. *Curr. Biol.* **12**, 13–25 (2002).
6. Mao, Y. S., Sunwoo, H., Zhang, B. & Spector, D. L. Direct visualization of the co-transcriptional assembly of a nuclear body by noncoding RNAs. *Nat. Cell Biol.* **13**, 95–101 (2011).
7. Wilusz, J. E. et al. A triple helix stabilizes the 3′ ends of long noncoding RNAs that lack poly(A) tails. *Genes Dev.* **26**, 2392–2407 (2012).
8. Naganuma, T. et al. Alternative 3′-end processing of long noncoding RNA initiates construction of nuclear paraspeckles. *EMBO J.* **31**, 4020–4034 (2012).
9. Nakagawa, S., Naganuma, T., Shioi, G. & Hirose, T. Paraspeckles are subpopulation-specific nuclear bodies that are not essential in mice. *J. Cell. Biol.* **193**, 31–39 (2011).
10. Li, R., Harvey, A. R., Hodgetts, S. I. & Fox, A. H. Functional dissection of NEAT1 using genome editing reveals substantial localization of the NEAT1_1 isoform outside paraspeckles. *RNA* **23**, 872–881 (2017).
11. Souquere, S., Beauclair, G., Harper, F., Fox, A. & Pierron, G. Highly ordered spatial organization of the structural long noncoding NEAT1 RNAs within paraspeckle nuclear bodies. *Mol. Biol. Cell* **21**, 4020–4027 (2010).
12. West, J. A. et al. Structural, super-resolution microscopy analysis of paraspeckle nuclear body organization. *J. Cell. Biol.* **214**, 817–830 (2016).
13. West, J. A. et al. The long noncoding RNAs NEAT1 and MALAT1 bind active chromatin sites. *Mol. Cell* **55**, 791–802 (2014).
14. Hirose, T. et al. NEAT1 long noncoding RNA regulates transcription via protein sequestration within subnuclear bodies. *Mol. Biol. Cell* **25**, 169–183 (2014).
15. Nakagawa, S. et al. The lncRNA Neat1 is required for corpus luteum formation and the establishment of pregnancy in a subpopulation of mice. *Development* **141**, 4618–4627 (2014).
16. Standaert, L. et al. The long noncoding RNA Neat1 is required for mammary gland development and lactation. *RNA* **20**, 1844–1849 (2014).
17. Imamura, K. et al. Long noncoding RNA NEAT1-dependent SFPQ relocation from promoter region to paraspeckle mediates IL8 expression upon immune stimuli. *Mol. Cell* **53**, 393–406 (2014).
18. Prasanth, K. V. et al. Regulating gene expression through RNA nuclear retention. *Cell* **123**, 249–263 (2005).
19. Chen, L. L., DeCerbo, J. N. & Carmichael, G. G. Alu element-mediated gene silencing. *EMBO J.* **27**, 1694–1705 (2008).
20. Elbarbary, R. A., Li, W., Tian, B. & Maquat, L. E. STAU1 binding 3′ UTR IRAlus complements nuclear retention to protect cells from PKR-mediated translational shutdown. *Genes Dev.* **27**, 1495–1510 (2013).
21. Hu, S. B. et al. Protein arginine methyltransferase CARM1 attenuates the paraspeckle-mediated nuclear retention of mRNAs containing IRAlus. *Genes Dev.* **29**, 630–645 (2015).
22. Torres, M. Circadian RNA expression elicited by 3′-UTR IRAlu-paraspeckle associated elements. *eLife* **5**, e14837 (2016).
23. Yin, Q. F. et al. SnoVectors for nuclear expression of RNA. *Nucleic Acids Res.* **43**, e5 (2015).
24. Gupta, S., Campbell, D., Derijard, B. & Davis, R. J. Transcription factor ATF2 regulation by the JNK signal transduction pathway. *Science* **267**, 389–393 (1995).
25. Lau, E. et al. PKCε promotes oncogenic functions of ATF2 in the nucleus while blocking its apoptotic function at mitochondria. *Cell* **148**, 543–555 (2012).
26. Biswas, G. et al. Retrograde Ca²⁺ signaling in C2C12 skeletal myocytes in response to mitochondrial genetic and metabolic stress: a novel mode of inter-organelle crosstalk. *EMBO J.* **18**, 522–533 (1999).
27. Quiros, P. M., Mottis, A. & Auwerx, J. Mitonuclear communication in homeostasis and stress. *Nat. Rev. Mol. Cell Biol.* **17**, 213–226 (2016).
28. Luz, A. L. et al. Deficiencies in mitochondrial dynamics sensitize *Caenorhabditis elegans* to arsenite and other mitochondrial toxicants by reducing mitochondrial adaptability. *Toxicology* **387**, 81–94 (2017).
29. Liu, S. et al. Oxidative stress and MAPK involved into ATF2 expression in immortalized human urothelial cells treated by arsenic. *Arch. Toxicol.* **87**, 981–989 (2013).
30. Tait, S. W. & Green, D. R. Mitochondria and cell death: outer membrane permeabilization and beyond. *Nat. Rev. Mol. Cell Biol.* **11**, 621–632 (2010).
31. Watkins, P. A., Maiguel, D., Jia, Z. & Pevsner, J. Evidence for 26 distinct acyl-coenzyme A synthetase genes in the human genome. *J. Lipid Res.* **48**, 2736–2750 (2007).
32. He, M. et al. Identification and characterization of new long chain acyl-CoA dehydrogenases. *Mol. Genet. Metab.* **102**, 418–429 (2011).
33. Yang, R. Z., Blaileanu, G., Hansen, B. C., Shuldiner, A. R. & Gong, D. W. cDNA cloning, genomic structure, chromosomal mapping, and functional expression of a novel human alanine aminotransferase. *Genomics* **79**, 445–450 (2002).
34. Cabreiro, F. et al. Overexpression of mitochondrial methionine sulfoxide reductase B2 protects leukemia cells from oxidative stress-induced cell death and protein damage. *J. Biol. Chem.* **283**, 16673–16681 (2008).

35. Scarpulla, R. C. Transcriptional paradigms in mammalian mitochondrial biogenesis and function. *Physiol. Rev.* **88**, 611–638 (2008).

36. Kara, C. J., Liou, H. C., Ivashkiv, L. B. & Glimcher, L. H. A cDNA for a human cyclic AMP response element-binding protein which is distinct from CREB and expressed preferentially in brain. *Mol. Cell. Biol.* **10**, 1347–1357 (1990).

37. Consortium, E. P. An integrated encyclopedia of DNA elements in the human genome. *Nature* **489**, 57–74 (2012).

38. Fox, A. H., Bond, C. S. & Lamond, A. I. P54nrb forms a heterodimer with PSP1 that localizes to paraspeckles in an RNA-dependent manner. *Mol. Biol. Cell.* **16**, 5304–5315 (2005).

39. Alvarez-Paggi, D. et al. Multifunctional cytochrome *c*: learning new tricks from an old dog. *Chem. Rev.* **117**, 13382–13460 (2017).

40. Jiang, X. & Wang, X. Cytochrome *c*-mediated apoptosis. *Annu. Rev. Biochem.* **73**, 87–106 (2004).

41. Zhu, J. P., Vinothkumar, K. R. & Hirst, J. Structure of mammalian respiratory complex I. *Nature* **536**, 354–358 (2016).

42. Lee, K., Kerner, J. & Hoppel, C. L. Mitochondrial carnitine palmitoyltransferase 1a (CPT1a) is part of an outer membrane fatty acid transfer complex. *J. Biol. Chem.* **286**, 25655–25662 (2011).

43. McGarry, J. D. & Brown, N. F. The mitochondrial carnitine palmitoyltransferase system. From concept to molecular analysis. *Eur. J. Biochem.* **244**, 1–14 (1997).

44. Labbe, K., Murley, A. & Nunnari, J. Determinants and functions of mitochondrial behavior. *Annu. Rev. Cell. Dev. Biol.* **30**, 357–391 (2014).

45. Engreitz, J. M., Ollikainen, N. & Guttman, M. Long non-coding RNAs: spatial amplifiers that control nuclear structure and gene expression. *Nat. Rev. Mol. Cell Biol.* **17**, 756–770 (2016).

46. Chen, L. L. Linking long noncoding RNA localization and function. *Trends Biochem. Sci.* **41**, 761–772 (2016).

47. Shin, Y. & Brangwynne, C. P. Liquid phase condensation in cell physiology and disease. *Science* **357**, eaaf4382 (2017).

48. Knott, G. J., Bond, C. S. & Fox, A. H. The DBHS proteins SFPQ, NONO and PSPC1: a multipurpose molecular scaffold. *Nucleic Acids Res.* **44**, 3989–4004 (2016).

49. Fox, A. H., Nakagawa, S., Hirose, T. & Bond, C. S. Paraspeckles: where long noncoding RNA meets phase separation. *Trends Biochem. Sci.* **43**, 124–135 (2018).

50. Yamazaki, T. et al. Functional domains of NEAT1 architectural lncRNA induce paraspeckle assembly through phase separation. *Mol. Cell* **70**, 1038–1053 (2018).

51. Chatel-Chaix, L. et al. Dengue virus perturbs mitochondrial morphodynamics to dampen innate immune responses. *Cell Host Microbe* **20**, 342–356 (2016).

Acknowledgements

Author contributions

L.-L.C. conceived of the study. Y.W., S.-B.H. designed the experiments. Y.W., S.-B.H., R.-W.Y. and D.W. performed experiments. M.-R.W. and L.Y. preformed bioinformatics analyses of RNAi screenings and RNA–seq data. L.-L.C., Y.W., S.-B.H. and M.-R.W analysed the data. L.-L.C. wrote the manuscript with input from the other authors.

Additional information

Supplementary information is available for this paper at https://doi.org/10.1038/s41556-018-0204-2.

Reprints and permissions information is available at www.nature.com/reprints.

Correspondence and requests for materials should be addressed to L.-L.C.

Publisher's note: Springer Nature remains neutral with regard to jurisdictional claims in published maps and institutional affiliations.

Methods

Plasmid construction and generation of stable cell lines. TALEN-mediated EGFP and poly(A) sequences knocking-in to the *NEAT1* promoter were designed and assembled as described in ref. [52]. The TALEN assembly kit was obtained from Addgene. The target sequences of the *NEAT1* TALEN plasmid are 5′-GACCCCGGTGACGCG-3′ and 5′-AGTTGTGGCAAGTCC-3′. The homologous arm sequences (chr11:65,421,968-65,422,789, chr11:65,422,798-65,423,623) for donor plasmids were amplified from the genomic DNA of HeLa cells, and the different regulatory modules (*EGFP* and the BGH/SV40 poly(A) sequences) were amplified from pEGFP-C1 and pLKO.1 vectors, followed by insertion into pCRII vector. Transfection of plasmids NEAT1-EGFP donor and *NEAT1* TALEN into HeLa cells was carried out with X-tremeGENE 9 Reagent (Roche). Single clones of NEAT1^G-HeLa were selected by fluorescence intensity and puromycin selection. To express mCherry in NEAT1^G -HeLa, pHAGE-EF1α-IRES-mCherry was cloned by the KOD-Plus Mutagenesis Kit (TOYOBO) and *mCherry* was amplified from pmCherry-C1. Lentiviral particles were produced in HEK293 cells by co-transfection of constructs pHAGE-EF1α-IRES-mCherry, psPAX2 and pMD2.G, followed by infection into NEAT1^G-HeLa cells. Single clones with an equivalent fluorescence intensity of EGFP and mCherry were selected as NEAT1^G-HeLa-R clones. Genomic DNA and total RNA of selected single clones were extracted for genotyping or *NEAT1* expression analyses.

pGL3-NEAT1-promoter was cloned by inserting the *NEAT1* promoter (2,000 bp upstream of *NEAT1* TSS) from gDNAs of HeLa cells into pGL3-Basic Vector (Promega) using XhoI/MluI. Deletion of the CRE site of the *NEAT1* promoter in pGL3-*NEAT1*-promoter was created with the Hieff MutTM Site-Directed Mutagenesis Kit (Yeasen).

To construct shRNA vectors, target sequences of the screening positive gene candidates and a scramble sequence were cloned into pLKO.1-TRC vector between the AgeI and EcoRI sites.

To generate double-allele *NEAT1* KO HeLa cell lines, six sgRNAs (three targeting upstream and three targeting downstream of the *NEAT1* gene) were designed and inserted into one CRISPR/Cas9-nuclease vector px330A with the Multiplex CRISPR/Cas9 Assembly System Kit (Addgene).

To generate Δp(A) HeLa cell lines, four sgRNAs (two targeting upstream and two targeting downstream of the *NEAT1_1* p(A) signal) were designed and inserted into vector pX330A (Addgene).

To express EGFP-NONO in BCL2 KD and Δp(A) deleted cells, the full-length NONO DNA sequence was amplified from cDNA of HeLa cells, and inserted into pEGFP-C1 vector. The primers used are listed in Supplementary Table 4.

Cell culture and transfection. HeLa and HEK293 cells were maintained in DMEM supplemented with 10% FBS and penicillin/streptomycin. Plasmid transfection was carried out with X-tremeGENE 9 (Roche) for HeLa and HEK293 cells with ~80–90% transfection efficiency in general.

Lentivirus production and cell infection. To produce lentiviral particles, 0.6×10^7 HEK293 cells were plated in a 10 cm dish for 24 h and then co-transfected with 10 μg pLKO.1, 7.5 μg psPAX2 and 3 μg pMD2.G. The supernatant containing viral particles was harvested twice at 48 and 72 h after transfection, filtered through a Millex-GP filter unit (0.45 μm pore size, Millipore), and stored at −80 °C until use. Cells were cultured in medium containing lentivirus and 1 μg ml^{-1} polybrene (Sigma) under infection and several days of puromycin selection was used to increase the knockdown efficiency.

Nuclear and cytoplasmic RNA fractionation, RNA isolation and RT–qPCR. Nuclear and cytoplasmic fractionation was carried out as described in ref. [21]. Total RNA from cultured cells was extracted with Trizol Reagent (Invitrogen). For RT–qPCR, after treatment with DNase I (Ambion, DNA-free kit), cDNA synthesis was carried out using SuperScript III (Invitrogen) with oligo (dT) and random hexamers. qPCR was performed using SYBR Green Realtime PCR Master Mix (TOYOBO) and a StepOnePlus real-time PCR system (Applied Biosystems). *Actin* mRNA was used for normalization. The relative expression of each examined gene was determined with triplicate independent experiments. Primers are listed in Supplementary Table 4.

Dual luciferase reporter assay. For the *NEAT1* promoter luciferase assay, shRNA knockdown and control cells were seeded in a 96-well plate and co-transfected with pGL3-NEAT1-promoter reporter and Renilla luciferase vector in the ratio of 10:1, and Renilla luciferase was used as an internal control for normalization. At 24 h after transfection, luciferase activity was measured using a Dual-Glo luciferase assay system (Promega).

RNase protection assay. Total RNA was prepared as described above. RPA was performed with an RPAIII kit (Ambion). In brief, total RNA (scramble, 30 μg; BCL2_KD, 40 μg) was hybridized with 2 ng digoxigenin (DIG)-labelled antisense RNA probe, which was synthesized with T7 RNA polymerase (Promega) at 42 °C for ~12–16 h after denaturation in denaturing buffer. RNase A/T1 digestion (×100 dilution) excluded unhybridized single-stranded RNA probes for 30 min at 37 °C.

The protected RNA fragments were separated by 8% PAGE containing 8 M urea and visualized by northern blots (DIG Northern Starter Kit, Roche).

Seahorse assay. A Seahorse assay was performed with the Seahorse XF^e Analyzer according to the manufacturer's instructions. HeLa cells (2×10^4) or HEK293 cells (4×10^4) were seeded on the XF^e 24 microplate and incubated overnight in normal growth medium, while the sensor cartridge was hydrated overnight. The next day, the medium was changed to bicarbonate-free low buffered assay medium (25 mM glucose, 2 mM sodium pyruvate, 2 mM glutamine) and incubated at 37 °C for 1 h. Compounds were added (final concentrations: 1 μM oligomycin, 0.5 μM FCCP, 1 μM rotenone and antimycin A) to the reagent ports of the sensor cartridge, and the sensor cartridge and XF^e 24 microplate were placed in the XF^e Analyzer to collect data.

Apoptosis assay. Cells were plated in 12-well plates at a density of 1.5×10^5 cells per well. Cells were treated at 50% confluence with 500 μM SA. The proportion of apoptotic cells was measured using an Annexin V-FITC Apoptosis Detection Kit (Vazyme) after 24 h. Cells were passaged through a mesh (40 μm) after staining, and then analysed on a BD LSRII SORP flow cytometer.

ChIP. HeLa cells (1×10^7) were harvested and suspended in 10 ml PBS with 1% formaldehyde to fix for 10 min at room temperature (r.t.). Crosslinking was quenched by the addition of glycine to a final concentration of 0.25 M, followed by incubation for 5 min at r.t. After pelleting cells at 1,000 r.p.m. for 5 min, the cell pellets were resuspended in 1 ml lysis buffer (50 mM Tris pH 8.0, 150 mM NaCl, 1 mM EDTA, 1% Triton X-100 (ABCONE), 0.1% sodium deoxycholate, phosphatase inhibitor cocktail III (MedChemExpress)), followed by sonication with an S220 Focused-Ultrasonicator (Covaris) to achieve 300–500 bp DNA fragments. After centrifugation at 16,000g for 10 min at 4 °C, the supernatant was precleared with 15 μl Dynabeads Protein G (Invitrogen) with 100 μg BSA and 100 μg ssDNA. Precleared lysates were then incubated overnight at 4 °C with 20 μl Dynabeads Protein G and 2 μg anti-ATF2, anti-p71-ATF2 antibody and rabbit IgG, individually. The beads were washed with 600 μl lysis buffer, 600 μl high salt wash buffer (1% Triton X-100, 0.1% sodium deoxycholate, 50 mM Tris-HCl at pH 8.0, 0.5 M NaCl, 5 mM EDTA), 600 μl LiCl immune complex wash buffer (0.25 M LiCl, 0.5% Igepal, 0.5% sodium deoxycholate, 10 mM Tris pH 8.0, 1 mM EDTA) sequentially, followed by two washes with 600 μl TE Buffer (10 mM Tris pH 8.0, 1 mM EDTA) at 4 °C. The complex was eluted by adding 200 μl freshly prepared elution buffer (1% SDS, 0.1 M NaHCO$_3$) with rotation at r.t. for 15 min. Reverse crosslinking was carried out by adding 8 μl 5 M NaCl and incubating at 65 °C for 4 h, followed by a supplement of 4 μl 0.5 M EDTA and 10 μl proteinase K (10 mg ml^{-1}) at 55 °C for 2 h. DNAs were purified for qPCR. Primers are listed in Supplementary Table 4, and antibodies are listed in Supplementary Table 5.

Native RNA immunoprecipitation. HeLa cells (2×10^7) were rinsed twice with ice-cold PBS and suspended in 1 ml RNA immunoprecipitation (RIP) buffer (50 mM Tris pH 7.4, 150 mM NaCl, 0.5% Igepal, 1 mM phenylmethyl sulfonyl fluoride (PMSF), 1× protease inhibitor cocktail (Roche) and 2 mM ribonucleoside vanadyl complex (VRC, NEB)) followed by sonication. Cell lysates were centrifuged at 1,000g for 10 min at 4 °C and the supernatants were precleared with 10 μl Dynabeads Protein G (Invitrogen). The precleared supernatants were then divided into two parts equally and incubated with 20 μl Dynabeads Protein G with antibodies for NONO or mouse IgG2b for 2 h at 4 °C, followed by washing three times with high salt buffer (RIP buffer with 0.5 M NaCl, 0.5% sodium deoxycholate and 0.1% Igepal) and twice with RIP buffer. The beads were incubated with elution buffer (100 mM Tris pH 6.8, 4% SDS, 10 mM EDTA) at r.t. for 10 min. One-third of the eluted sample was used for western blot and the remainder was used for RNA extraction. Antibodies are listed in Supplementary Table 5.

***NEAT1* CHART.** *NEAT1* CHART was carried out as described in ref. [53] with the probes indicated in Supplementary Fig. 4a. Probes targeting *egfp* were used as mock. HeLa cells (2×10^7) were crosslinked with 2 mM disuccinimidyl glutarate (Thermo) at r.t. for 45 min and 3% formaldehyde at 37 °C for 10 min. Crosslinking was quenched by the addition of glycine to a final concentration of 0.25 M followed by incubation at r.t. for 5 min. After spinning at 1,000 r.p.m. for 5 min, the cell pellets were resuspended in 1 ml lysis buffer (10 mM HEPES (ABCONE) pH 7.5, 20 mM NaCl, 1.5 mM MgCl$_2$, 1 mM EDTA, 1 mM dithiothreitol (DTT), 1 mM PMSF, 0.1% NP40). Cells lysates were transferred into an ice-cold glass dounce for homogenization by douncing followed by spinning at 3,300× g for 7 min. After removing supernatant, nuclei were re-suspended in WB100 buffer (10 mM HEPES pH 7.5, 100 mM NaCl, 1 mM PMSF, 0.1% N-lauroylsarcosine, 40 U ml^{-1} RNasin) followed by sonication with an S220 Focused-Ultrasonicator (Covaris) (100 PW, 20% duty cycle, 200 burst, 1.5 min, 4 °C). The lysate was digested with DNase at 37 °C for 15 min and stopped by adding 10 mM EDTA and 5 mM EGTA. The lysate was precleared with 50 μl streptavidin C-1 magnetic beads at 4 °C for 20 min. The precleared lysates were hybridized with 350 nM probes at r.t. for 6 h followed by the addition of 150 μl strepavidin C-1 magnetic beads and incubation overnight at r.t. The beads were washed with WB250 buffer (10 mM HEPES pH 7.5, 250 mM NaCl, 0.2% SDS, 1 mM EGTA, 2 mM EDTA, 1 mM PMSF, 0.1% N-lauroylsarcosine) four

times for 5 min each, and then digested by proteinase K at 50 °C for 1 h followed by boiling for 10 min. Finally, 500 μl Trizol was added for RNA isolation.

FRAP. Cells were cultured on 29 mm no.1.5 glass-bottomed dishes (Cellvis). Plasmid pEGFP-NONO was transfected 24 h before imaging (for BCL2 KD cells, transfection was carried out after cells were treated with BCL2 shRNAs for 72 h). Photobleaching and subsequent image acquisition (10 prebleached images, and a sequence of post-bleach images at 200 images every 1 s) were performed on a Leica TSC SP8 STED 3X. Data were calculated as described in ref. [54] and fitted in a one-phase exponential association curve by GraphPad Prism7.

FISH and SIM. For all SIM visualization of *NEAT1*, cells were seeded on high performance no. 1.5 (18 × 18 mm) glass coverslips (Schott Nexterion), fixed and permeabilized as described in ref. [55]. To visualize *NEAT1*, cells were incubated in 50% formamide/2× SSC at r.t. for 10 min. A set of Cy3/488-labelled nick translation and denatured probes targeting *NEAT1* were added and hybridized at 37 °C in a humid chamber for 16 h. Unbound probes were washed away by 50% formamide/2× SSC, nuclei were counterstained with 4,6-diamidino-2-phenylindole. Primers for probes are list in Supplementary Table 4. SIM observation was carried out as described in ref. [56].

To visualize mitochondria in living cell, cells were cultured on 29 mm no. 1.5 glass-bottomed dishes (Cellvis). Staining of mitochondria was carried out with MitoTracker Deep Red FM – Special Packaging (Invitrogen) according to the manufacturer's protocol. Cells were washed once with PBS and the medium was replaced by FluoroBrite DMEM (GIBCO) supplemented with 10% FBS and placed back in the incubator for 1 h. For imaging of the single time point, sections with 0.125 μm spacing were acquired.

smFISH. All smFISH probes were designed via Stellaris Probe Designer and labelled with cy3 (*cycs, cpt1a, ndufa13, actin*) or cy5 (*neat1*) on 3′ ends. Briefly, cells were fixed with 4% PFA for 15 min, followed by permeabilization with 0.5% Triton X-100 for 5 min. Cells were incubated in 10% formamide/2× SSC for 10 min at r.t. follow by hybridization at 37 °C for 16 h. Samples were mounted in ProLong Diamond antifade reagent (Thermo Fisher).

Imaging analysis of paraspeckle, mitochondria and smFISH. Analyses of paraspeckle morphology were performed with SIM images. Images were measured by Imaris using the surface building system. The parameter sphericity was used to analyse the proportion of paraspeckle morphology and the distribution was referred to a previous description[12]. Paraspeckle numbers were analysed with images taken by a DeltaVision Elite imaging system. Images were cropped and processed by Fiji/ImageJ followed by calculation with Image-Pro Plus.

To collect the statistics of mitochondrial morphology, living cell imaging of mitochondria was carried out by SIM, and signals were visualized and deconvoluted with a DeltaVision Elite imaging system (GE Healthcare). Classification of elongated and fragmented mitochondria was carried out according to refs [51,57].

Due to the limited resolution in wide-field microscopy, we introduced a parameter named 'elongation rate (Er = 1/sphericity − 1)' to distinguish globular or elongated paraspeckles. As the linear regression of the individual volume and Er of paraspeckles showed a high positive correlation (Supplementary Fig. 5a), we defined paraspeckles as globular or elongated using their volumes, calculated by signals of *NEAT1* smFISH captured via wide-field microscopy. A total of 50 globular or elongated paraspeckles were selected, and the signal intensities of *NEAT1*-enriched mito-mRNAs in individual paraspeckles were calculated by Imaris software to compare the retention capacity of globular and elongated paraspeckles.

To measure changes in mito-mRNAs retained in paraspeckles following FCCP and oligomycin treatments, the co-localization foci of each *NEAT1*-enriched mito-mRNA in globular paraspeckles were counted for DMSO, FCCP and oligomycin treatments, respectively.

ATP viability assay. Cells were plated in 96-well plates at a density of 1.5×10^4 cells per well and were allowed to grow for 14 h at 37 °C in a humidified 5% CO_2 atmosphere. The amount of ATP in cells was measured using a luciferase-based CellTiter-Glo Luminescent Cell Viability Assay (Promega). The relative ATP viability was normalized to HeLa WT cells.

Cell proliferation assay. WT and *NEAT1*_KO HeLa cells (2×10^3) were seeded in 96-well plates and cell numbers were measured every 24 h by a CellTiter 96 Aqueous One Solution Cell Proliferation Assay (Promega). The cell numbers were normalized to those in 0 h cells.

Genome-wide RNAi screening of human genes associated with *NEAT1* promoter. For RNAi screening, the human ON-TARGETplus (OPT) siRNA library (GE Dharmacon) targeting 18,104 genes was used to screen potential genes that have an impact on *NEAT1* transcription. Briefly, before transfection, RNAi MAX transfection reagent (0.1 μl RNAi MAX in each well) was added to 384-well plates in which each well contained four siRNAs targeting one single gene. After

20 min, NEAT1^G-HeLa-R cells were seeded at a density of 500 cells per well. Cells were cultured for 72 h to knock down gene expression. After washing with PBS using an LS405 microplate (BioTek), the fluorescence intensities of mCherry and EGFP were measured, recorded and analysed using Operetta (PerkinElmer). Two independent experiments were performed.

Analysis of genome-wide RNAi screening. Raw data were supported by Operetta. The ratio$_{EGFP/mCherry}$ was calculated to indicate the level of *NEAT1* transcription. Two replicates were highly correlated (Pearson correlation coefficient = 0.9565) and were merged to identify regulators of *NEAT1* transcription (Supplementary Fig. 1a-d). A permutation test was performed to compute *P* values[58] on ratio$_{EGFP/mCherry}$ averaged across replicates. Genes with normalized fluorescence$_{EGFP}$ < 0.8, normalized fluorescence$_{mCherry}$ > 0.8, ratio$_{EGFP/mCherry}$ < 0.67 and *P* < 0.05 were considered as candidates that enhance *NEAT1* transcription. Genes with normalized fluorescence$_{EGFP}$ > 1.2, normalized fluorescence$_{mCherry}$ < 1.2, ratio$_{EGFP/mCherry}$ > 1.5 and *P* < 0.05 were considered as candidates that suppress *NEAT1* transcription. Only genes expressed in HeLa cells were further considered as candidates.

RNA–seq and differentially expressed gene analysis. RNA–seq libraries were prepared using Illumina TruSeq mRNA Sample Prep Kit V2 and subjected to deep sequencing with Illumina X ten. High-throughput sequencing read quality was evaluated by FastQC (v0.11.7). Raw fastq files were trimmed using Trimmomatic (v0.36) to remove sequencing adapter and low quality reads, then mapped to human GRCh38/hg38 genome using HISAT2 (v2.0.5, —max-seeds 20 –k 10)[59]. FPKM of each gene was calculated using featureCounts (v1.5.2)[60]. Differentially expressed gene analysis of two *NEAT1* KO lines were compared with WT HeLa cells, respectively, with a fold change of FPKM$_{KO}$/FPKM$_{WT}$ > 2.

***NEAT1* CHART–RNA-seq.** For each sample, CHART–RNA-seq was performed in one deep sequencing from three independent CHART experiments. Libraries were prepared using an Illumina TruSeq RNA Sample Preparation Kit v2 and were subjected to deep sequencing with an Illumina HiSeq 2000 at CAS-MPG Partner Institute for Computational Biology Omics Core (Shanghai). High-throughput sequencing read quality was evaluated by FastQC (v0.11.7). Raw fastq files were first mapped to the human GRCh38/hg38 genome using HISAT2[59]. Then MACS (v2.1.1, —bw 200 -m 5 50)[61] was used to call peaks between *NEAT1* CHART–RNA and mock samples based on the statistical model of MACS. Peaks with $P < 1 \times 10^{-5}$ were selected as statistically significant peaks. BEDTools[62] was used to determine genes enriched by *NEAT1* CHART–RNA based on selected peaks. Final gene candidates were obtained by removing false positive genes that are not expressed in HeLa cells.

GO analysis. To classify screening candidates based on their functions and subcellular location patterns, we used AmiGO 2[63] to annotate GO terms of candidates, with a manual check to remove unfaithful annotations. For mito-mRNAs enriched in *NEAT1* CHART–RNA-seq, we used Ingenuity Pathway Analysis (IPA, QIAGEN) to generate the network maps. To identify *NEAT1*-enriched RNA motifs, we performed MEME[64] with full-length sequences of mito-mRNAs enriched by *NEAT1* CHART–RNA-seq.

Statistics and reproducibility. The data used in this study are presented as mean ± s.d. or s.e.m. Statistical analyses (two-sided Student's *t*-test, linear regression, correlation analysis and so on) were performed using existing software (GraphPad Prism 7, R and MACS). *P* < 0.05 was considered significant. Representative pictures for FISH, FRAP, immunofluorescence and western blotting were obtained from at least two independent experiments. For the statistical significance and sample size of all graphs, please see figure legends and Methods for details. Raw data and precise *P* values are provided in Supplementary Table 6 and unprocessed blots are provided in Supplementary Fig. 8.

Reporting Summary. Further information on research design is available in the Nature Research Reporting Summary linked to this article.

Data availability

RNAi screening data reported in this Article have been deposited at PubChem BioAssay with AID 1259429. All sequencing data, including RNA–seq and CHART–RNA–seq, have been deposited at the Gene Expression Omnibus (GEO) under accession no. GSE110775. Source data for statistics in Figs. 1–8 and Supplementary Figs. 2, 3 and 5–7 are provided in Supplementary Table 6. All other data supporting the findings of this study are available from the corresponding author on reasonable request.

References

52. Cermak, T. et al. Efficient design and assembly of custom TALEN and other TAL effector-based constructs for DNA targeting. *Nucleic Acids Res.* **39**, e82 (2011).
53. Simon, M. D. et al. The genomic binding sites of a noncoding RNA. *Proc. Natl Acad. Sci. USA* **108**, 20497–20502 (2011).

54. Dundr, M. et al. A kinetic framework for a mammalian RNA polymerase in vivo. *Science* **298**, 1623–1626 (2002).

55. Wu, H. et al. Unusual processing generates SPA lncRNAs that sequester multiple RNA binding proteins. *Mol. Cell* **64**, 534–548 (2016).

56. Xing, Y. H. et al. SLERT regulates DDX21 rings associated with Pol I transcription. *Cell* **169**, 664–678 (2017).

57. Zhang, Y. et al. Mitoguardin regulates mitochondrial fusion through MitoPLD and is required for neuronal homeostasis. *Mol. Cell* **61**, 111–124 (2016).

58. Good, P. I. *Permutation Tests: A Practical Guide to Resampling Methods for Testing Hypotheses* 2nd edn, Vol. 63 (Springer, New York, 2001).

59. Kim, D., Langmead, B. & Salzberg, S. L. HISAT: a fast spliced aligner with low memory requirements. *Nat. Methods* **12**, 357–360 (2015).

60. Liao, Y., Smyth, G. K. & Shi, W. featureCounts: an efficient general purpose program for assigning sequence reads to genomic features. *Bioinformatics* **30**, 923–930 (2014).

61. Feng, J., Liu, T., Qin, B., Zhang, Y. & Liu, X. S. Identifying ChIP-seq enrichment using MACS. *Nat. Protoc.* **7**, 1728–1740 (2012).

62. Quinlan, A. R. & Hall, I. M. BEDTools: a flexible suite of utilities for comparing genomic features. *Bioinformatics* **26**, 841–842 (2010).

63. Carbon, S. et al. AmiGO: online access to ontology and annotation data. *Bioinformatics* **25**, 288 (2009).

64. Bailey, T. L., Williams, N., Misleh, C. & Li, W. W. MEME: discovering and analyzing DNA and protein sequence motifs. *Nucleic Acids Res.* **34**, W369–W373 (2006).

nature research

Corresponding author(s):   Ling-Ling Chen

Reporting Summary

Nature Research wishes to improve the reproducibility of the work that we publish. This form provides structure for consistency and transparency in reporting. For further information on Nature Research policies, see Authors & Referees and the Editorial Policy Checklist.

Statistical parameters

When statistical analyses are reported, confirm that the following items are present in the relevant location (e.g. figure legend, table legend, main text, or Methods section).

n/a	Confirmed	
☐	☒	The exact sample size (*n*) for each experimental group/condition, given as a discrete number and unit of measurement
☐	☒	An indication of whether measurements were taken from distinct samples or whether the same sample was measured repeatedly
☐	☒	The statistical test(s) used AND whether they are one- or two-sided *Only common tests should be described solely by name; describe more complex techniques in the Methods section.*
☒	☐	A description of all covariates tested
☒	☐	A description of any assumptions or corrections, such as tests of normality and adjustment for multiple comparisons
☐	☒	A full description of the statistics including central tendency (e.g. means) or other basic estimates (e.g. regression coefficient) AND variation (e.g. standard deviation) or associated estimates of uncertainty (e.g. confidence intervals)
☐	☒	For null hypothesis testing, the test statistic (e.g. *F*, *t*, *r*) with confidence intervals, effect sizes, degrees of freedom and *P* value noted *Give P values as exact values whenever suitable.*
☒	☐	For Bayesian analysis, information on the choice of priors and Markov chain Monte Carlo settings
☒	☐	For hierarchical and complex designs, identification of the appropriate level for tests and full reporting of outcomes
☐	☒	Estimates of effect sizes (e.g. Cohen's *d*, Pearson's *r*), indicating how they were calculated
☐	☒	Clearly defined error bars *State explicitly what error bars represent (e.g. SD, SE, CI)*

Our web collection on statistics for biologists may be useful.

Software and code

Policy information about availability of computer code

Data collection	BD FACSDiva v 6.1.2 software was used for collection of flow cytometry data. Fluorescent images were acquired with softWoRx 6.5 (GE).
Data analysis	For imaging analyses, Fiji Image J, Image pro plus (v6.0) and Imaris (v8.4.1) were used. GraphPad Prism7, R (v3.3.2) and Microsoft Excel 2016 were used for statistical analysis and graphing, HISAT2 (v2.0.5) for mapping sequencing data to genome, MACS (v2.1.1) for peak calling, BEDTools (v2.19.0) for identifying enriched genes, featureCounts (v1.5.2) for FPKM calculation and FlowJo v 10 for flow cytometry data analyses.

For manuscripts utilizing custom algorithms or software that are central to the research but not yet described in published literature, software must be made available to editors/reviewers upon request. We strongly encourage code deposition in a community repository (e.g. GitHub). See the Nature Research guidelines for submitting code & software for further information.

Data

Policy information about [availability of data](#)

All manuscripts must include a [data availability statement](#). This statement should provide the following information, where applicable:

- Accession codes, unique identifiers, or web links for publicly available datasets
- A list of figures that have associated raw data
- A description of any restrictions on data availability

The main data supporting the findings of this study are available within the article and its Supplementary Information files. All other data supporting the findings of this study are available from the corresponding author upon reasonable request. RNAi screening data reported in this paper have been deposited at PubChem BioAssay with AID:1259429. The sequencing data supporting the findings of this study have been deposited in NCBI Gene Expression Omnibus under accession codes GSE:110775, dataset will be publicly available after the manuscript is accepted.

Field-specific reporting

Please select the best fit for your research. If you are not sure, read the appropriate sections before making your selection.

☒ Life sciences ☐ Behavioural & social sciences ☐ Ecological, evolutionary & environmental sciences

For a reference copy of the document with all sections, see [nature.com/authors/policies/ReportingSummary-flat.pdf](#)

Life sciences study design

All studies must disclose on these points even when the disclosure is negative.

Sample size	Sample size determination used in FISH, FRAP and other graphs were described as previous published study and experimental knowledge.
Data exclusions	Data from knockdown experiments were excluded in which shRNA showed little KD efficiency.
Replication	The experimental findings in all figures were reproduced successfully.
Randomization	FISH and FRAP images for statistical analyses were randomly selected.
Blinding	Blinding was not possible because we used cells/cell lines in our experiments. The chemical treatments and samples harvest process made it impossible to be blinded. And blinding was not relevant to our study, because we used cultured cells and all data were collected by apparatus equipment with no human bias involved.

Reporting for specific materials, systems and methods

Materials & experimental systems

n/a	Involved in the study
☒	Unique biological materials
☐	Antibodies
☐	Eukaryotic cell lines
☒	Palaeontology
☒	Animals and other organisms
☒	Human research participants

Methods

n/a	Involved in the study
☒	ChIP-seq
☐	Flow cytometry
☒	MRI-based neuroimaging

Antibodies

Antibodies used	For all antibodies, their supplier name, catalog number, clone name and dilution are provided in Supplementary Table 5.
Validation	Validation statement for each primary antibody is provided on the manufacture's website.

Eukaryotic cell lines

Policy information about cell lines

Cell line source(s)	Information and references for used cells (HeLa, HEK293 and U2OS) are provided in the manuscript.
Authentication	The cell lines have been used in the lab for over 3 years, so authentications were not performed.
Mycoplasma contamination	All cell lines have been tested for mycoplasma contamination free by PCR method.
Commonly misidentified lines (See ICLAC register)	No cell lines used in this study were found in the database of commonly misidentified cell lines that is maintained by ICLAC and NCBI Biosample.

Flow Cytometry

Plots

Confirm that:

☒ The axis labels state the marker and fluorochrome used (e.g. CD4-FITC).

☒ The axis scales are clearly visible. Include numbers along axes only for bottom left plot of group (a 'group' is an analysis of identical markers).

☒ All plots are contour plots with outliers or pseudocolor plots.

☒ A numerical value for number of cells or percentage (with statistics) is provided.

Methodology

Sample preparation	Cultured cells were collected by trypsinization and operated according to manufacturer's instruction. Cells were suspended in single-cell condition after passage through a mesh (40 µm) after staining.
Instrument	BD LSRII SORP
Software	FlowJo v 10
Cell population abundance	For data collection: BD FACSDiva v 6.1.2 software; for data analysis: FlowJo v 10.
Gating strategy	After cells were selected in the FSC/SSC dot plot to remove debris, gates of Annexin V+ and PI+ cells were set and compared with a control sample with no staining.

☒ Tick this box to confirm that a figure exemplifying the gating strategy is provided in the Supplementary Information.